JGR Atmospheres

RESEARCH ARTICLE

Key Points:

- Based on in situ data obtained at 6,523 m above sea level, the glacier surface energy balance and its atmospheric controls are examined
- Clouds governed the surface energy balance by decreasing the incident solar radiation less than increasing the incoming longwave radiation
- The dominant energy sinks shift from sublimation/evaporation on highly continental glaciers to melting on maritime/subcontinental glaciers

Correspondence to:

D. Zhang and M. Ding,
dqzhang@cma.gov.cn;
dingminghu@foxmail.com

Monsoon Clouds Control the Summer Surface Energy Balance on East Rongbuk Glacier (6,523 m Above Sea Level), the Northern of Mt. Qomolangma (Everest)

Weigang Liu[1,2] , **Dongqi Zhang[2]** , **Xiang Qin[3]**, **Michiel R. van den Broeke[4]** , **Youyan Jiang[5], Diyi Yang[6], and Minghu Ding[2,3]**

[1]Key Laboratory of Arid Climatic Change and Reducing Disaster of Gansu Province, Key Open Laboratory of Arid Climate Change and Disaster Reduction of CMA, Institute of Arid Meteorology, China Meteorological Administration, Lanzhou, China, [2]State Key Laboratory of Severe Weather and Institute of Tibetan Plateau & Polar Meteorology, Chinese Academy of Meteorological Sciences, Beijing, China, [3]State Key Laboratory of Cryospheric Science, Northwest Institute of Eco-Environment and Resources, Chinese Academy of Sciences, Lanzhou, China, [4]Institute for Marine and Atmospheric Research, Utrecht University, Utrecht, The Netherlands, [5]Lanzhou Regional Climate Center, Lanzhou, China, [6]Haining Meteorological Bureau, Haining, China

Abstract To identify the atmospheric controls of the summertime glacier surface energy balance in the Himalayas, in situ meteorological data collected at 6,523 m above sea level during May–July 2005 were obtained and analyzed. Our results showed that net shortwave radiation (103 W m^{-2}) and turbulent sensible heat flux (12 W m^{-2}) acted as energy sources, and net longwave radiation (-62 W m^{-2}) and turbulent latent heat flux (-20 W m^{-2}) represented heat sinks. Cloud cover controlled the summer surface energy balance. During the active period of the South Asian Summer Monsoon, the frequent cloud coverage increased the incoming longwave radiation more than it decreased the incident solar radiation. Intensification (weakening) of the South Asian Summer Monsoon strengthened (suppressed) surface melting. The melt energy measured during the nonmonsoon period was small due to the energy consumption associated with glacier volume warming, energy loss from sublimation, and large heat loss through net longwave radiation due to the low amount of incoming longwave radiation caused by the low cloudiness. The comparison of glacier surface energy balances on the Tibetan Plateau shows that on continental glaciers, net radiation is lower and accounts for a smaller contribution to energy sources, and the dominant energy sinks are sublimation and evaporation, rather than melting, which is the primary energy sink for maritime/subcontinental glaciers. This implies an important spatial variability in glacial sensitivity to different climatic conditions on the Tibetan Plateau.

1. Introduction

The largest glacier area outside the Arctic and Antarctic is found on the Tibetan Plateau and its surrounding regions (TP) (Xu et al., 2009). These glaciers are located at the headwaters of many prominent Asian rivers (e.g., Ganges, Indus, Brahmaputra, and Yangtze), which supply water for billions of people living downstream (Barnett et al., 2005; Xu et al., 2009). Glaciers are excellent indicators of climate change (Francou et al., 2005). Over the past few decades, because of climate warming (Qin et al., 2009; You et al., 2010), most glaciers on the TP experienced a negative mass balance and rapid shrinkage (Pellicciotti et al., 2015; Ren et al., 2004; Wagnon et al., 2013; Xiao et al., 2007; W. Yang et al., 2016; Yao et al., 2007, 2012; Ye et al., 2015, 2017), with the most negative mass balances occurring in the Himalayas (Yao et al., 2012), thereby endangering the water supply from Asia's water tower.

Glaciers are products of the surrounding climate, and their evolutions depend on climatic settings. For example, for the maritime glaciers in the monsoon-influenced southeast TP, the energy/mass budgets are particularly sensitive to the progression of the South Asian Summer Monsoon (SASM) (W. Yang et al., 2011); while in the Karakorum Mountains and the north TP, glaciers are stable or advancing (Agarwal et al., 2017; Scherler et al., 2011; Zhou et al., 2017), which can be attributed to the more intense continental climate (W. Yang et al., 2011) and strengthened westerlies (Yao et al., 2012). To accurately predict the response of glaciers to present and future climate changes, the physical interaction between glacier and atmosphere needs to be better understood. The glacier surface energy balance (SEB) is one way to describe this relationship (Mölg

& Hardy, 2004; Sun et al., 2018; W. Yang et al., 2013). To date, a variety of glacier SEB experiments have been conducted on mountainous glaciers and ice sheets around the world (Ding et al., 2020; Favier et al., 2004; Mölg & Hardy, 2004; Sun et al., 2012, 2014, 2018; Wagnon, Ribstein, Francou, & Pouyaud, 1999; Wagnon, Ribstein, Kaser, & Berton, 1999; Wal & Oerlemans, 1994; W. Yang et al., 2011; G. Zhang et al., 2013), including on debris-covered glaciers (Brock et al., 2010; Carenzo et al., 2016; Reid & Brock, 2010). These studies show how the glacier SEB differs in different climates.

On the TP, a few glacier SEB studies have been carried out previously, such as on the Chongce glacier in the western Kunlun mountains (Takahashi et al., 1989), the Xiaodongkemadi glacier in the Tanggula mountains (Y. Zhang et al., 1996), the Zhadang glacier in the Nyainqentanglha mountains in central Tibet (G. Zhang et al., 2013; Zhu et al., 2015), the Qiangtang No. 1 glacier in the inland TP (S. Li et al., 2018), the Laohugou No. 12 glacier in the Qilian mountains in the northeast TP (Sun et al., 2012, 2014, 2018), and the Parlung No. 4 glacier in southeast Tibet (W. Yang et al., 2011). However, detailed SEB studies observations are still limited in the Himalayas, especially at high-altitude sites. One took place on the Khumbu glacier and was conducted in 1999 in the southern Himalayas (Kayastha et al., 2000; Takeuchi et al., 2000), and the other took place on Xixiabangma glacier and was carried out in 1991 (Aizen et al., 2002) in the northern Himalayas. However, these two studies failed to describe instruments and technical specifications of the meteorological sensors in detail and simplified the turbulent heat flux calculations, which might prevent the evaluation of SEB accuracy and the drawing of general conclusions. Recently, detailed SEB measurements with eddy correlation system were conducted on Lirung glacier in 2016 (Steiner et al., 2018) and on Yala glacier from October 2016 to April 2017 (Stigter et al., 2018) in the southern Himalayas. Both studies emphasized the importance of the turbulent heat fluxes on the glacier energy and mass balances. However, SEB research on the northern Himalayas is still limited.

The Himalaya region is one of the most glacierized regions on Earth (Azam et al., 2018). It has a glacier cover of approximately 22,800 km^2 (Bolch et al., 2012), among which 8,202 km^2 are in China (Mi & Xie, 2002). Mt. Qomolangma (Everest) is the highest point of the Himalayas (8,848 m a.s.l.), lying on the border between China and Nepal, central Himalayas. Three peaks above 8,000 m a.s.l. and 10 peaks higher than 7,000 m a.s.l. surround it. The high altitude makes this area an intensively glacierized region. The local climate is dominated by the SASM in summer but by the midlatitude westerlies in winter. For the mountain glaciers at Mt. Qomolangma, the glacier mass balance depends fundamentally on the temperature and precipitation conditions of summer (Hou et al., 2000). As such, this region is an ideal location for studying the interaction between the atmosphere and glacier surfaces. Nevertheless, owing to the difficult logistic supply and harsh environment, knowledge of glacier SEBs around Mt. Qomolangma is incomplete.

The Rongbuk glacier is the largest glacier on the northern slope of Mt. Qomolangma. In May–July 2005, a glacio-meteorological campaign was carried out at 6,523 m a.s.l. in the accumulation zone of the Rongbuk glacier. This paper uses the meteorological data obtained in this field experiment to analyze the SEB and to investigate its atmospheric drivers. Additionally, the phenomenological links between variations in SEB components and the advancement of SASM are examined. The remainder of this paper is organized as follows: Section 2 outlines the observational site and experimental program, followed by Sections 3 and 4, which introduce the data treatment and methodology, respectively; Section 5 shows the robustness of the SEB equation used in this study; Section 6 highlights the results, which are further discussed in Section 7; and Section 8 presents conclusions.

2. Study Region and Measurement Program

The Rongbuk glacier (Figure 1) is a subcontinental glacier situated on the northern slope of Mt. Qomolangma in the central Himalayas (Liu et al., 2010). It consists of three tributaries, that is, the East, the West and the Central Rongbuk glaciers, with a total area of about 148 km^2 (X. Yang et al., 2015; Ye et al., 2009). The glacier surface has a discontinuous debris cover, with debris thicknesses ranging from several meters near 5,200 m a.s.l. (near the terminus) to several centimeters at approximately 6,000 m a.s.l. (Ye et al., 2015). In the glacier's low part, ice cliffs develop; in the high area (>6,000 m a.s.l.), seracs exist. Supra-glacier lakes are located on the debris-covered glacier tongue, with a total lake area and number increasing from 0.05 km^2 and 16 in 1971 to 0.71 km^2 and 87 in 2008 (Ye et al., 2009). The equilibrium line altitude (ELA) is
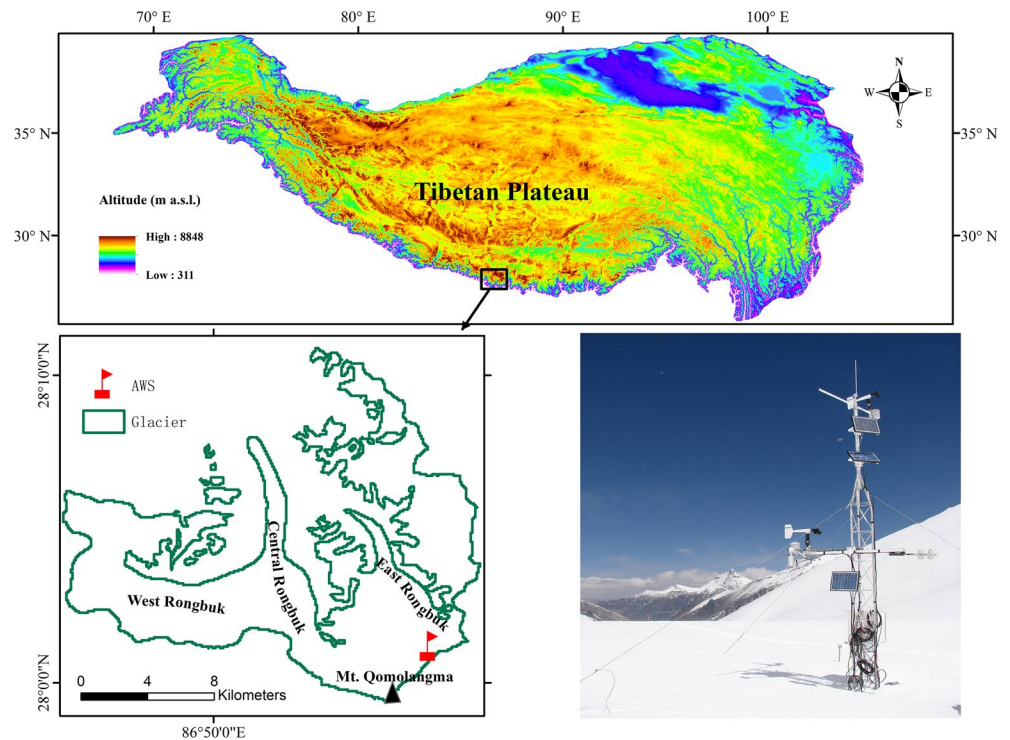
Figure 1. Locations of Rongbuk glacier and the AWS at 6,523 m a.s.l. AWS, automatic weather station.

situated between 5,800 and 6,200 m a.s.l., at which altitude the mean annual precipitation was estimated to be 500–800 mm water equivalent (w.e.), and the mean annual air temperature was estimated to range from −9 °C to −6 °C (Shi, 2005). The annual net accumulation (i.e., surface mass balance) derived from the East Rongbuk ice core (27°59′ N, 86°55′ E, 6,500 m a.s.l.) (Dahe et al., 2017) showed a sharp decrease in the annual mass balance from the mid-1950s (around 700 mm w.e.) to the late 1960s (450 mm w.e.), and a subsequent stabilization of approximately 450 mm w.e. (Hou et al., 2002), which is consistent with the substantially reduced amount of rainfalls over India from the mid-1950s to the late 1960s. The average annual accumulation values during 1954–1963 and 1964–1997 were 582 and 321 mm w.e., respectively, which are comparable with the 2000–2001 annual surface mass balance value of 498 mm w.e. measured using stakes at 6,500 m a.s.l. (D. Zhang et al., 2004). The snow pit record showed an annual accumulation rate of 296 mm w.e. near our automatic weather station (AWS) from summer 2008 to the spring 2009 (JianZhong Xu, 2016).

Compared to the prevailing continental climatic conditions in the inland TP (e.g., glaciers Xiaodongkemadi, Zhadang and Qiangtang No. 1) and the meteorological circumstance influenced by the East Asian monsoon on the eastern margin of the TP (e.g., Laohugou No.12 glacier), the local climate around the Rongbuk glacier is under the combined control of SASM and the westerlies. The period from June to September denotes the wet season, during which SASM prevails and the climate is wet, containing more than 80% of the annual precipitation falling (Cannon et al., 2015; M. Wang, 1962), while the period October-May is the dry season, during which the westerlies dominate and the weather is clear and dry with low precipitation. From 1959 to 2007, the mean annual air temperature at 4,300 m a.s.l. (Tingri county) on the northern slope of Mt. Qomolangma increased at a rate of 0.62 °C per decade, with the greatest warming trend in winter and the smallest in summer (X. Yang, Zhang, et al., 2011).

On May 1, 2005, an AWS was set up and operated at an altitude of 6,523 m a.s.l. on a relatively flat and open surface of East Rongbuk glacier (28°1′N, 86°57′E) (Figure 1). It was allowed to melt down freely with the glacier surface, which ensures a relatively constant height of the instruments above the glacier surface during melting. Continuous data sets were recorded from May 1 to July 22, 2005. Air temperature and humidity, together with the wind speed and direction, were measured at two heights, 1.5 and 2.5 m, respectively. The sensors for air temperature and relative humidity measurements were naturally ventilated

Table 1
Technical Specifications of the Automatic Weather Station's Sensors and Installation Heights

Elements	Sensor type	Accuracy (calibration range)	Installation height (in m)
Air temperature (°C)	Vaisala HMP 45D	±0.2 °C (−40 °C–60 °C)	1.5, 2.5
Relative humidity (%)	Vaisala HMP 45D	±2% (0.8%–100%)	1.5, 2.5
Wind speed (m s^{-1})	Young 05103	±0.3 m s^{-1} (0–100 m s^{-1})	1.5, 2.5
Wind direction (°)	Young 05103	±3° (0–355°)	1.5, 2.5
Air pressure (hPa)	PTB210	±0.35 Pa (50–1,100 hPa)	0.5
Incident solar radiation (W m^{-2})	K&Z CNR1	±10% for daily totals	1.5
Reflected shortwave radiation (W m^{-2})	K&Z CNR1	±10% for daily totals	1.5
Incoming longwave radiation (W m^{-2})	K&Z CNR1	±10% for daily totals	1.5
Outgoing longwave radiation (W m^{-2})	K&Z CNR1	±10% for daily totals	1.5

and shielded from solar radiation. Incident solar radiation $S{\downarrow}$, reflected shortwave radiation $S{\uparrow}$, incoming longwave radiation $L{\downarrow}$ and outgoing longwave radiations $L{\uparrow}$ were measured at 1.5 m, with radiation sensors perpendicular to the surface and that were leveled horizontally. The AWS was checked for sensor leveling, and data were downloaded every 3–5 days during the field experiment. A CR 1000 data logger from Campbell Scientific Inc., USA (with a low temperature resistance of −55 °C) connected all the sensors and recorded ten-minute data averages based on samples taken every 1 min. Technical specifications of the meteorological sensors, together with their installation heights, are shown in Table 1. During the intensive melting period from 10 June to 22 July, the surface mass balance (SMB) near the AWS was obtained using nine bamboo stakes, and snow density and solid precipitation (P) were also measured. Surface ablation was calculated with P - SMB. Beijing time (BJT), which is 2 h 12 min earlier than the local time (LT), was used throughout the whole experiment.

3. Data Treatment

Referring to Sun et al. (2018), Favier et al. (2004), Obleitner and De Wolde (1999), we processed the raw data we obtained. First, spurious data (only nine data points) in the raw meteorological data set were deleted, and then the occasionally missing data (three data points), together with the deleted data above, were linearly interpolated using their neighboring values. Second, we performed $S{\uparrow}$ corrections based on the method suggested by Favier et al. (2004) since radiation was generally affected by snow cover and rime on the dome of the radiation sensors and therefore needed calibration (van den Broeke et al., 2004). Third, following Obleitner and De Wolde (1999), we conducted $L{\downarrow}$ corrections for a window heating offset from the absorption of $S{\downarrow}$. Finally, all the recorded 10-min data were averaged into half-hourly values and used as input to solve the SEB equation. The correction process of $S{\uparrow}$ and $L{\downarrow}$ are detailed in Section 4.1.

4. Methods

By defining a volume extending from the glacier surface to a depth where the vertical heat flux is nonsignificant and ignoring horizontal energy transfer, the glacier SEB can be written as follows (in W m^{-2}), where the fluxes toward the glacier surface are defined positive (Oke, 1987):

$$S + L + H + LE + G + P = \Delta Q_m + \Delta Q_s = \Delta Q, \tag{1}$$

where S is the net shortwave radiation ($S = S{\downarrow} + S{\uparrow}$), L is the net longwave radiation ($L = L{\downarrow} + L{\uparrow}$), and H and LE are the turbulent sensible and latent heat fluxes, respectively. G is the conductive subsurface heat flux and can be computed from the one-dimensional temperature-depth profile from the glacier surface to a depth of 20 m. Its value is given by $G = -K_T \dfrac{\partial T}{\partial z}$, where K_T is thermal conductivity, which is 2.2 W m^{-1} K^{-1} for pure ice and 0.4 W m^{-1} K^{-1} for old snow (Oke, 1987). The observed ice temperature at a depth of 20 m

was nearly stable at -9.80 °C. P, the heat added to the surface by liquid precipitation, is insignificant in comparison to the other terms (Favier et al., 2004; Wagnon, Ribstein, Francou, & Pouyaud, 1999) because the near-surface air temperature was well below 0 °C at the observational site for most of the observation period; therefore liquid precipitation hardly occurred, and P is neglected in our study. ΔQ_m is the heat used to melt snow and ice, and ΔQ_s is the rate of gain/loss of heat of a vertical column extending from the surface to the depth at which seasonal variations in temperature are negligible (Paterson, 1994). ΔQ, the sum of ΔQ_m and ΔQ_s, corresponds to a temperature change within the surface layers if the very top layers of the glacier have temperatures below 0 °C (i.e., $\Delta Q_s = \Delta Q$) or is used to melt snow and ice if these layers are at 0 °C (i.e., $\Delta Q_m = \Delta Q$) (Favier et al., 2004). The SEB was calculated at half-hourly intervals.

4.1. Net All-Wave Radiation

The net all-wave radiation R is the sum of S and L:

$$R = S + L = S\downarrow + S\uparrow + L\downarrow + L\uparrow, \tag{2}$$

where $S\downarrow$, $S\uparrow$, $L\downarrow$ and $L\uparrow$ are radiation fluxes directly measured by the AWS (Table 1). The glacier surface albedo can be defined as $\alpha = -S\uparrow/S\downarrow$; and therefore, Equation 2 can also be written as $R = S\downarrow(1-\alpha) + L\downarrow + L\uparrow$.

Considering that $\alpha = 0.9$ is the realistic maximum and $S\uparrow$ might be affected by the surface inclination and snowfalls covering the pyranometer, $S\uparrow = -S\downarrow \times 0.9$ is applied for a systematic $S\uparrow$ correction in case of $-S\uparrow > S\downarrow \times 0.9$, which was previously adopted by Favier et al. (2004). Additionally, heating of the pyranometer dome by solar radiation can result in large $L\downarrow$ recordings (Weiss, 1981). Therefore, to reduce the influence of incident solar radiation on $L\downarrow$, $L\downarrow$ is corrected based on the method suggested by Obleitner and De Wolde (1999):

$$L\downarrow = L\downarrow - k \times S\downarrow, \tag{3}$$

where k is a correction coefficient. $k = 2.7\%$ was found in the dry conditions of the Sahel (Culf & Gash, 1993), but a smaller k of 1.2% was adopted by Obleitner and De Wolde (1999) on Vatnajökull, which is the major ice cap in Iceland. $k \approx 2\%$ was observed by analyzing $L\downarrow$ measurements under a shadowing ring and analyzing $L\uparrow$ measurements on a melting surface of Zongo glacier in the Bolivian Andes (Sicart, 2005). Given that the Rongbuk and Zongo glaciers are both mountainous glaciers located in mid-latitudes, the k value used on Zongo glacier (2%) was adopted in this study. In addition, since the glacier surface temperature maximum is 0 °C, the measured $L\uparrow$ was limited to a maximum value of 315.6 W m^{-2} with the assumption that the surface longwave emissivity is 1.

4.2. Turbulent Heat Fluxes Calculation

4.2.1. Bulk Aerodynamic Method

Based on the Monin-Obukhov similarity theory, the bulk aerodynamic method with a stability correction can be applied to calculate turbulent heat fluxes (Oke, 1987). Compared to the profile method, the bulk aerodynamic method is less sensitive to measurement uncertainties and thus is more appropriate for application on sloping glacier surfaces where katabatic winds prevail and the wind speed maximum can fall just within a few meters above the glacier surface (Denby & Greuell, 2000). This method only needs one level of meteorological measurement, although it requires input for surface roughness variables (Arck & Scherer, 2002). Atmospheric stability within the surface layer can be described by the bulk Richardson number R_{ib}, which relates the relative effects of buoyancy to the mechanical generation of turbulence (Daniel Moore, 1983; Oke, 1987):

$$R_{ib} = \frac{g\frac{\Delta T}{\Delta Z}}{T\left(\frac{\Delta u}{\Delta z}\right)^2} = \frac{g(T - T_s)(z - z_{om})}{Tu^2}, \tag{4}$$

where T is air temperature (in K); u is horizontal wind speed (in m s^{-1}), where T and u are measured; z is the height (in m); g is the acceleration of gravity ($g = 9.81$ m s^{-2}); and T_s is the surface temperature (in K). z_{om}, the surface roughness length for momentum (in m), is a fictitious height at which the horizontal wind speed can be extrapolates to zero. Positive (negative) R_{ib} values represent stable (unstable) atmospheric stratification.

Assuming that the local gradients of mean horizontal wind speed, mean air temperature and mean specific humidity are equal within the finite differences between the measurement level and glacier surface, analytical expressions for turbulent heat fluxes can be calculated as follows (Oke, 1987):

$$H = \rho \frac{C_p u k^2 \left(T - T_s\right)}{\left(\ln \dfrac{z}{z_{om}}\right)\left(\ln \dfrac{z}{z_{ot}}\right)}\left(\Phi_m \Phi_h\right)^{-1},$$

(5)

$$LE = \rho \frac{L_s u k^2 \left(q - q_s\right)}{\left(\ln \dfrac{z}{z_{om}}\right)\left(\ln \dfrac{z}{z_{oq}}\right)}\left(\Phi_m \Phi_v\right)^{-1},$$

(6)

where ρ is the air density at 6,523 m a.s.l. and was calculated based on the measured air temperatures (T) and air pressures; C_P is the specific heat capacity of air at constant pressure and can be estimated by $C_P = C_{Pd}\left(1 + 0.84q\right)$, with the specific heat capacity for dry air at a constant pressure of $C_{Pd} = 1005$ J kg^{-1} k^{-1}. L_s (2.834×10^6 J kg^{-1}) is the latent heat of sublimation for snow/ice when the glacier surface temperature $T_s < 273.15$ K, or the latent heat of evaporation (2.501×10^6 J kg^{-1}) when $T_s = 273.15$ K (i.e., glacier surface is melting). k is the von Karman constant (0.4); q is air specific humidity (in kg kg^{-1}) and can be obtained using the observed relative humidity and air temperature values; q_s, the specific humidity (in kg kg^{-1}) at the glacier surface, can be obtained under the assumption of a saturated glacier surface; and T_s, the glacier surface temperature, is calculated from the Stefan-Boltzmann equation $L \uparrow = \sigma T_s^4$ ($\sigma = 5.67 \times 10^{-8}$ W m^{-2} K^{-4}) (Favier et al., 2004; Wagnon et al., 2003) under the assumption that the snow/ice emissivity is unity. z_{om}, z_{ot}, and z_{oq} are surface roughness lengths for momentum, temperature and humidity, respectively (in m). Φ_m, Φ_h, and Φ_v are nondimensional stability functions for momentum, heat and moisture, respectively. They can be expressed in terms of R_{ib} (Brutsaert, 1982; Oke, 1987):

For $R_{ib} > 0$ (stable atmosphere):

$$\left(\Phi_m \Phi_h\right)^{-1} = \left(\Phi_m \Phi_v\right)^{-1} = \left(1 - 5R_{ib}\right)^2,$$

(7)

For $R_{ib} < 0$ (unstable atmosphere):

$$\left(\Phi_m \Phi_h\right)^{-1} = \left(\Phi_m \Phi_v\right)^{-1} = \left(1 - 16R_{ib}\right)^{0.75},$$

(8)

4.2.2. Roughness Lengths

To calculate H and LE, the surface roughness lengths, that is, z_{om}, z_{oq}, and z_{ot}, must be known. Many previous studies have revealed that z_{oq} and z_{ot} were 1 or 2 orders of magnitude smaller than z$_{om}$ (Andreas, 1987, 2002; Morris, 1989; Munro, 1989), except for the work conducted in Antarctica by King and Anderson (1994), who found z_{ot}, z_{oq} >> z_{om}. z_{om} can be estimated by wind profile method, eddy covariance measurement, micro-topography and energy-balance closure method (Brock et al., 2006). In this study, the scheme proposed by Brock et al. (2006) was adopted to compute z_{om} as this scheme has been demonstrated to be robust for z_{om} calculation on glacier surface. Following Brock et al. (2006), only the wind speed observations meeting the following criteria were used in the iterative process for the z_{om} calculation: (1) the wind speed at the higher AWS level exceeds that at the lower level and (2) nonobstructed airflow exceeds fetches of at least 500 m. In view of the topography near the AWS (Figure 1), this criterion can be met by only choosing the wind with

directions ranging from 270° to 360° (northwest wind) and from 135° to 180° (southeast wind) because there was no airflow obstruction in these direction ranges. Further criteria include the follows: (3) wind speeds at the higher level are larger than 3.5 m s^{-1}, which ensures a well-mixed turbulent flow; and (4) the atmosphere is near-neutral, which is indicated by $-0.03 < R_{ib} < 0.03$.

The z_{ot} and z_{oq} values were often set to be equal to z_{om} in many previous glacier SEB studies (Brock et al., 2010; Favier et al., 2004; Mölg & Hardy, 2004; Wagnon et al., 2003; Wagnon, Ribstein, Kaser, & Berton, 1999). This is reasonable because (1) several SEB investigations have showed that it is appropriate to set equal roughness lengths for smooth glacier surfaces (Brock et al., 2010; Favier et al., 2004; Mölg & Hardy, 2004; Sicart, 2005; Wagnon et al., 2003; Wagnon, Ribstein, Francou, & Pouyaud, 1999; W. Yang et al., 2011) and (2) the theoretical framework suggests using equal roughness lengths if the difference between them is unknown (Bintanja & Reijmer, 2001). However, some schemes were also proposed to parameterize the Z_{ot} and Z_{oq} values, such as the schemes proposed by K. Yang et al. (2002), Smeets and van den Broeke (2008), and Andreas (1987). In this study, the parameterization scheme proposed by Andreas (1987) is adopted for z_{ot} and z_{oq} calculations since it was specially calibrated using data over snow and sea ice and has been successfully implemented on many glaciers, such as Tibetan glaciers (Guo et al., 2011; Sun et al., 2018; W. Yang et al., 2011) and the largest Austrian glacier, the Pasterze glacier (Greuell & Smeets, 2001). Following Andreas (1987), the roughness Reynolds number ($Re_* = \dfrac{u^* z_{om}}{v}$, where $v = 1.16 \times 10^{-5}$ m s^{-1} is the kinematic viscosity of air) is introduced to describe the aerodynamic flow regime. More details of this parameterization scheme can be referenced to Andreas (1987). Finally, the calculated z_{om}, z_{ot}, and z_{oq} values are averaged.

4.2.3. Ablation Calculation

As a residual energy component, ΔQ is consumed by glacier melting when T_s reaches 273.15 K. The half-hourly glacier melting amount is calculated as follows:

$$M = \frac{\Delta Q \Delta t}{\rho L_f} \left(\text{when } T_s = 273.15 \text{ K} \right), \tag{9}$$

where M is the half-hourly glacier melting (in m) with no consideration of refreezing, ρ is water density (1,000 kg m^{-3}), L_f is the latent heat of fusion (3.34×10^5 J kg^{-1}), and Δt (in s) is 30 min, that is, 1,800 s. The work conducted on Xiaodongkemadi glacier on the TP by Fujita et al. (2017) found that in the accumulation zone for the period May–September, about 60% of meltwater was trapped by refreezing. As meltwater refreezing was not observed on the East Rongbuk glacier, the refreezing rate of 60% on Xiaodongkemadi glacier was assumed in this study. Therefore, the meltwater was calculated as 0.4 M.

In addition to glacier melting, mass exchange at the glacier surface also consists of sublimation/deposition (riming) and evaporation/condensation, which are all associated with the turbulent latent heat flux (LE). The surface temperature (T_s) and the sign of LE determine which occurs at the glacier surface. Negative LE indicates mass loss in the form of sublimation and evaporation, while positive LE represents mass gains through deposition and condensation. The mass exchange associated with LE is computed as follows:

$$\text{when } T_s = 273.15 \text{ K } W_{\text{eva}} = \frac{-LE \, \Delta t}{\rho L_e} \text{ (if } LE < 0) \tag{10}$$

$$W_{\text{con}} = \frac{LE \, \Delta t}{\rho L_e} \quad \text{(if } LE > 0), \tag{11}$$

$$\text{when } T_s < 273.15 \text{ K } W_{\text{sub}} = \frac{-LE \, \Delta t}{\rho L_s} \text{ (if } LE < 0), \tag{12}$$
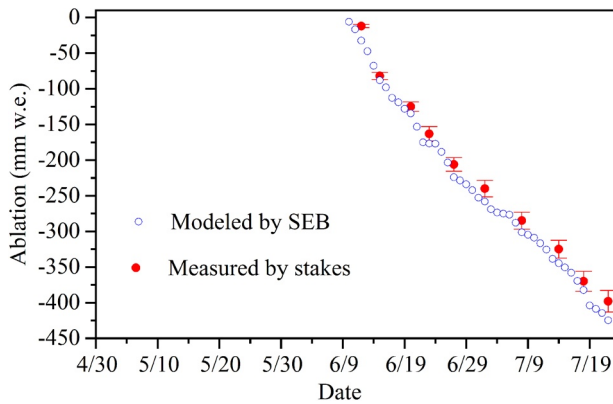
Figure 2. Cumulative daily ablation values measured by ablation stakes and derived from the SEB model from June 10 to July 22, 2005. SEB, surface energy balance.

$$W_{dep} = \frac{LE \, \Delta t}{\rho L_s} \, (\text{if } LE > 0), \tag{13}$$

where W_x is the mass exchange amount (in m), with the subscript x of eva, con, sub, and dep denoting evaporation, condensation, sublimation, and deposition, respectively, and L_e (2.501×10^6 J Kg^{-1}) and L_s (2.834×10^6 J Kg^{-1}) are the latent heat of evaporation and sublimation, respectively. The ablation total computed by the SEB is the sum of 0.4 M, sublimation/evaporation and condensation/deposition.

5. Ablation Validation

To evaluate the robustness of the SEB model used in this study, the cumulative ablation data derived from stake and precipitation measurements (called measured ablation hereafter) from 10 June to 22 July were compared with those calculated by the SEB method (Figure 2). Ablation was strongly suppressed by significant snowfall events on 21 and 23 June, and on 5 and 6 July. From 10 June to 22 July, the calculated ablation total was 425 mm w.e. at the AWS, exceeding the manually measured ablation by 30 mm w.e. (~7%). This discrepancy is acceptable in view of the standard deviation of 12 mm for the ablation measurement by the nine ablation stakes. In addition, Sun et al. (2014) stated that the underestimation of the turbulent heat fluxes calculation by the bulk aerodynamic method can also lead to underestimation of ablation calculation. Overall, it appears that the energy components involved in the SEB model consists of the primary processes and can give a good simulation of the energy- and mass-balance of the East Rongbuk glacier.
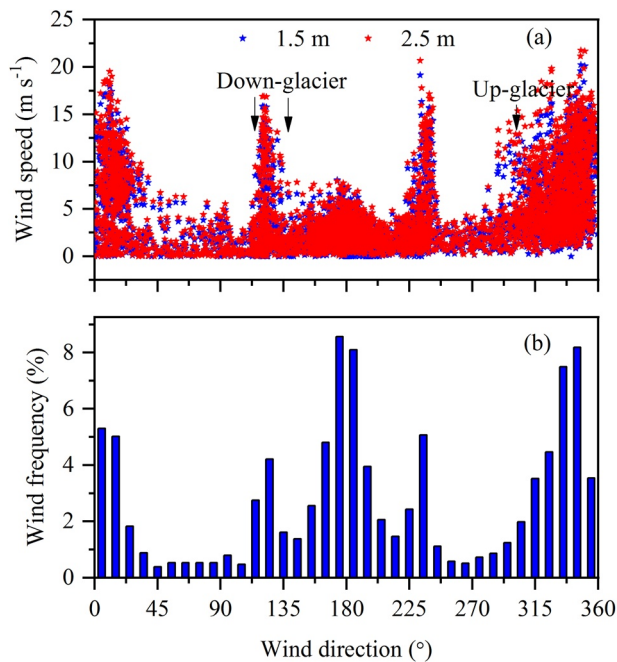
6. Results

Figure 3. (a) Scatter plot of the half-hourly wind speed versus wind direction and (b) histogram showing the frequencies of the half-hourly wind direction binned into 10° intervals.

6.1. Glacio-Meteorological Conditions

The half-hourly wind observations are summarized in Figure 3. Katabatic winds (90° < direction < 180°) alternated with the up-glacier winds (270° < direction < 360°) (Figure 3a), with direction frequencies of 35% and 37%, respectively (Figure 3b). Before 1 June, wind speeds not only had high values, but also had remarkable variations. Subsequently, however, they became low and varied slightly. The maximum observed half-hourly wind speed was 21.8 m s^{-1} (Figure 3a). The daily average wind speeds at 2.5 m ranged from 1.2 to 16.1 m s^{-1}, with an overall average of 4.6 m s^{-1} (Figure 4a).

The observed relative humidity (*RH*) averaged 60%. Before 1 June, daily *RH* values were typically low, with values in late May even reaching below 20%; subsequently, *RH* increased notably to values above 60%; toward the end of July, the daily average *RH* increased to more than 80%. Daily specific humidity values in the air (q) and at the glacier surface (q_s) are shown in Figure 4b. They had nearly similar ascending trends, although the daily q_s values were always slightly above the daily q throughout the whole observation period, except for two days (5 May and 7 July). They both experienced an increase from approximately 2 g kg^{-1} in early May to approximately 6 g kg^{-1} in late July. As observation went on, the difference between them decreased. The largest moisture difference occurred in late May (>2 g kg^{-1}), and the smallest difference was in July (approximately 0.5 g kg^{-1}).
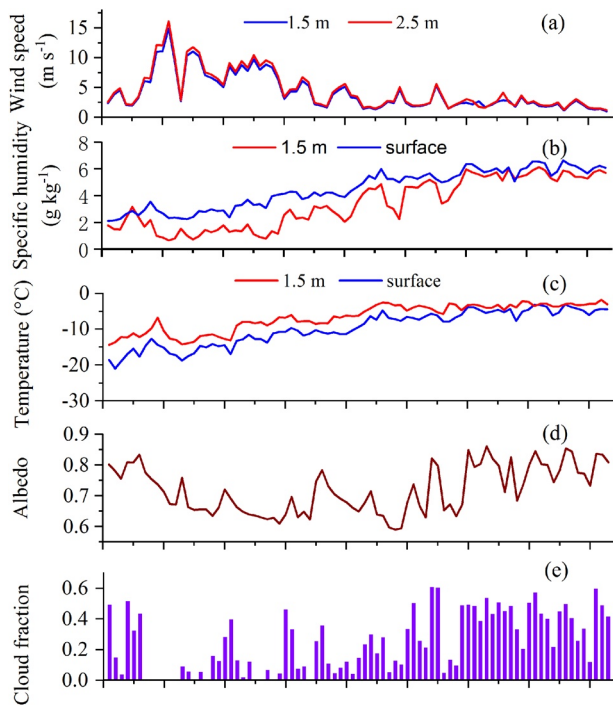
Figure 4. Daily averaged (a) wind speed, (b) specific humidity, (c) temperature, (d) surface albedo, and (e) cloud fraction from May 1 to July 22, 2005.

The observed daily mean air temperatures persistently surpassed the surface temperatures during most of the observation period (Figure 4c), with values always below the melting point of ice (0 °C) and with averages of −6.7 °C and −9.8 °C, respectively. Both of them gradually increased from early to late June and then varied little with nearly constant values. The temperature gradient between surface and air decreased, with a maximum gradient over 7.6 °C at the beginning of the observation period to a minimum of 0.4 °C during the last few days. A typical vertical temperature profile observed on 10 June 2005 is shown in Figure 5. During the night, the surface layer was stable ($R_{ib} > 0$), similar to that observed on the debris-free Zongo glacier, Bolivia (Sicart, 2005) and on the debris-covered Miage glacier, Italian Alps (Brock et al., 2010). During daytime, the atmosphere became unstable ($R_{ib} < 0$), likely as a result of the radiative heating of the snow surface, which is also observed over polar ice sheets (van den Broeke, 1997). Brock et al. (2010) attributed the daytime atmospheric instability over Miage glacier to the low wind speeds and steep temperature gradient present between surface and the observational height.

By dividing the daily $S\uparrow$ by the daily $S\downarrow$, the daily surface albedo values were obtained (Figure 4d). From 1 May to 18 June, the albedo mostly declined, likely owing to dry snow metamorphism (grain growth), excluding a few episodes of increase, for example, 1–3 May, 13 May, 20 May, 5 June, and 13 June, during which the albedo rapidly increased, probably because of snowfalls. After 18 June, however, albedo variability increased, which might be the combined result of more frequent snowfalls and intense ablation leading to rapid metamorphism and snow darkening. The average albedo from 1 May to 18 June was 0.69, which was lower than the average value of 0.77 after 18 June.

The study region is influenced by the SASM (Zou et al., 2009); therefore, cloudy weather prevails during the monsoon period. Following the method proposed by Favier et al. (2004), $n = 1.3 - 1.4(S\downarrow/S_{TOA})$ was used for the cloud cover estimation, where n is the cloud fraction and S_{TOA} is solar radiation at the top of the atmosphere (calculated using a solar constant of 1368 W m^{-2}). The cloud cover obtained is shown in Fig-
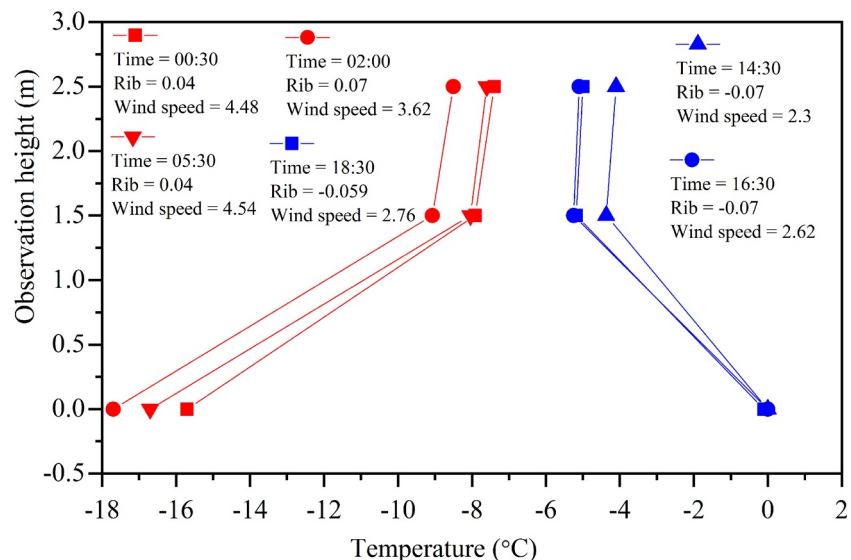

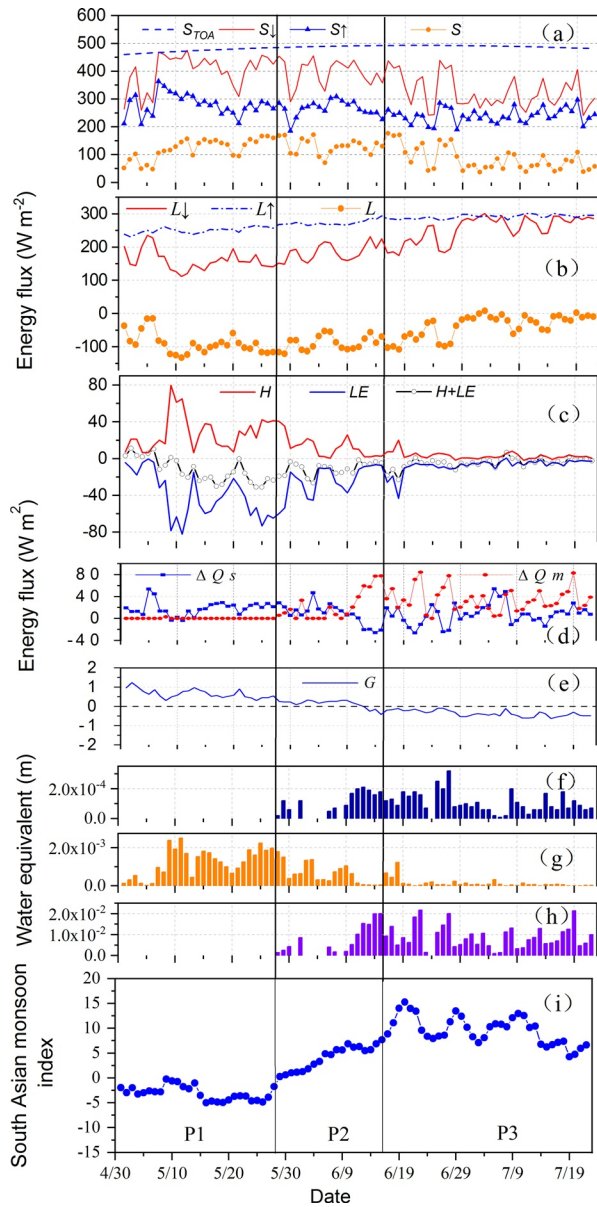**Figure 5.** Vertical temperature profile on June 10, 2005.

Figure 6. Variations in (a) shortwave radiation, (b) longwave radiation, (c) turbulent heat fluxes, (d) surface energy budget, (e) conductive flux, (f) evaporation, (g) sublimation, (h) melting, and (i) the three period according to the South Asian summer Monsoon index.

ure 4e. Before 19 June, the local weather was mainly dominated by clear-sky conditions, with an average fraction of 0.15; after 19 June, however, cloud cover increased, reaching a mean cloud fraction of 0.40. In addition, comparing Figure 4d with Figure 4e, it can be seen that period with high/low variability in the cloud fraction before/after 19 June commonly correspond to periods with high/low albedo variabilities.

Following the method shown in Section 4.2.2, 44 half-hourly profiles met the criteria, and a single z_{om} was generated from each, giving a mean z_{om} value of 0.9 mm, which was then used to compute z_{ot} and z_{oq}. The mean values of $z_{ot} = 0.035$ mm and $z_{oq} = 0.042$ mm were obtained and used as inputs for Equations 5 and 6 for the H and LE calculations. Brock et al. (2007) summarized z_{om} values on glaciers worldwide. They concluded that on mid-latitude glaciers, z_{om} over smooth fresh snow surfaces was generally on the order of 0.1 mm. On a polar snow surface, however, z_{om} was generally lower, with typical values of 0.01 mm, though some were even smaller 0.001 mm. z_{om} values on Tibetan glaciers have also been reported in recent years. On the Parlung No. 4 glacier in southwestern Tibet, z_{om} generally varied on orders of 0.1–10 mm (Guo et al., 2011), with average values of 0.3 mm for smooth snow surface and 0.8 mm for rough surface (W. Yang et al., 2011). On Laohugou No. 12 glacier in the northeast edge of the TP, monthly values determined by an eddy-covariance system on the bare ice ranged from 1.2 to 1.8 mm from June to September (Sun et al., 2018). By calibrating sublimation values measured in field, z_{om} values of 2.9 mm on the Antizana glacier (Favier et al., 2004) and 0.5–1 mm on the Illimani glacier (Wagnon et al., 2003) in the tropical Andes were obtained. The mean z_{om} of 0.9 mm obtained in this study is comparable to those reported above.

6.2. Shortwave Radiation

The amount of downward shortwave radiation theoretically possible at the observational latitude of Rongbuk glacier (28°1′N) is quite large and is close to the extraterrestrial value. Aizen et al. (2002) noted that without atmospheric effects (reflection and absorption of clouds, etc.), such high radiation inputs should prohibit the existence of glaciers at these latitudes. Figure 6a shows variations in daily $S\downarrow$, $S\uparrow$, S, and S_{TOA}. Daily $S\downarrow$ ranged from 241 to 476 W m^{-2}, with an average of 366 W m^{-2}, and had a high interdiurnal variability. Compared to the second half of the observational period, the $S\downarrow$ values in the first half were higher, which was very likely a result of the clear-sky conditions in the first half, as seasonal changes in extraterrestrial solar radiation (S_{TOA}) are small at low latitudes during such a short 3-month period. The daily $S\uparrow$ magnitudes ranged between 185 and 364 W m^{-2}, and had an average value of 259 W m^{-2}. Its sharp magnitude increase generally corresponded to abrupt albedo increase (Figure 4d). The net shortwave radiation S ranged from 37 to 176 W m^{-2}, with an average value of 107 W m^{-2}, representing the most influential heat source at the glacier-atmosphere interface.

6.3. Longwave Radiation

The daily longwave radiation fluxes $L\uparrow$, $L\downarrow$, and L are shown in Figure 6b. $L\uparrow$ showed a positive trend. Corresponding largely to the mean daily surface temperature range from −21.0 °C to −3.1 °C, daily $L\uparrow$ ranged from −231 to −302 W m^{-2}, with an average of −274 W m^{-2}. In comparison to $L\uparrow$, $L\downarrow$ had a larger variability with magnitudes generally smaller than $L\uparrow$. $L\downarrow$ ranged from 112 to 301 W m^{-2} and had a daily average of

208 W m^{-2}. The clear-sky emissivity term follows variations in atmospheric temperature and humidity. Before mid-June, the $L\downarrow$ values were relatively low (170 W m^{-2}) due to the prevailing cold-dry environment. After that, $L\downarrow$ increased considerably because of the warmer and wetter air (Figures 4b and 4c) and more frequent clouds (Figure 4e). The standard deviations of $L\downarrow$ before/after mid-June were 31 and 39 W m^{-2}, respectively.

L was negative and acted as a persistent energy sink for the glacier surface throughout most of the observational period, except in the last few days in July when L was close to zero (less than 8 W m^{-2}). L thus exhibited a markedly positive trend, with values ranging from -133 W m^{-2} in the beginning to $+8$ W m^{-2} toward the end, with an average of -66 W m^{-2}. The averaged daily L before and after mid-June were -90 W m^{-2} and -35 W m^{-2}, respectively. The coefficients of variation in $L\downarrow$ was 26%, 19% higher than that in $L\uparrow$. Therefore, changes in L were mainly dependent on changes in $L\downarrow$.

6.4. Turbulent Heat Fluxes

The turbulent heat fluxes, including those of H, LE and $H + LE$, are shown in Figure 6c. Compared to S and L mentioned above, H and LE were relatively small in magnitude. The daily average H ranged from -2 to 80 W m^{-2}, and the daily averaged LE ranged between 1 and -82 W m^{-2}, with averages equaling to 13 and -22 W m^{-2}, respectively. The magnitudes of H and LE not only maintained identical decreasing trends but also nearly canceled out. In the stable surface layer that prevailed during the observational period, the turbulence intensity greatly depended on wind speeds (Equations 5 and 6), which explains the synchronous decrease in the magnitude of H and LE with declining wind speeds. The variations in H and LE were large before late May but small after mid-June. Their daily summed values of $H + LE$ were close to zero in the last few observational days mainly because of the weak wind (Figure 4a). The positive H value obtained during most of the observation period indicated that H was an energy source and supplied energy to warm glacier. However, the negative LE implied its role as a persistent and significant energy sink.

6.5. Melting Energy and Conductive Heat Flux

The melting energy ΔQ_m, energy convergence/divergence for sensible heat ΔQ_s and the conductive heat flux G are shown in Figures 6d and 6e, respectively. Glacier melting does not happen until both the following criteria are met: $\Delta Q > 0$ W m^{-2} and $T_s = 0$ °C. During the majority of the observational days before 28 May, daily ΔQ represented positive ΔQ_s and there was no melting energy ΔQ_m. The daytime internal energy gains caused by variations in radiation and heat conduction surpassed the nighttime energy losses, and thus, there was energy convergence within the glacier volume, which was mainly used to warm the glacier volume and increase surface temperature. After 28 May, as more energy was absorbed by the glacier surface, surface temperatures increased more frequently to the melting point, especially at noon. Melting occurred almost every day. Under such conditions of glacier melting, ΔQ was composed of both melting energy ΔQ_m and energy convergence/divergence ΔQ_s. Negative ΔQ_s also appeared during the time when there was intensive melting, which illustrated that under the warm conditions of melting occurrence, the nighttime energy losses caused by variations in radiation and heat conduction were larger than the daytime energy gains, exerting an overall cooling effect on the glacier volume, thereby decreasing snow/ice temperature at a daily time scale during these days. The averaged ΔQ_m and ΔQ_s values were 11 and 21 W m^{-2}, respectively. The net radiation R (i.e., $S + L = 43$ W m^{-2}) provided the largest contribution (128%) to ΔQ, followed by the turbulent sensible heat H (13 W m^{-2}, 42%).

G contributed a minor portion to the glacier SEB, with daily values always near 1 W m^{-2}. In mid-June, G shifted from positive to negative. Before that time, melting scarcely occurred, and G was positive and directed toward the surface and gradually diminished to zero in mid-June. During this period, the glacier surface cooled. After mid-June, however, G turned to be negative, and its direction pointed away from the glacier surface.

Table 2
Surface Energy Balance Components and Their Respective Contributions at 6,523 m asl on East Rongbuk Glacier From May 1 to July 22, 2005

Month	Input (W m⁻²)			Output (W m⁻²)				Input (%)			Output (%)			
	S	H	G	L	LE	ΔQ	G	S	H	G	L	LE	ΔQ	G
May	123	28	1	−92	−40	−19	–	82	18	0	61	27	13	–
June	121	7.0	–	−76	−16	−36	0	95	5	–	59	13	28	0
July[a]	65	2.0	–	−18	−4	−45	0	97	3	–	26	7	67	0
Average	103	12	0	−62	−20	−33	–	89	11	0	54	18	29	–

[a]Mean values from 1 to 22 July.

6.6. Glacial Surface Energy Balance

Based on the surface energy balance components calculated above, the glacial surface energy balance was estimated (Table 2). S provided near 90% of the energy, followed by H with a share of approximately 10%. The conductive heat flux G only represented a minor energy source with a very small share of less than 1%. Although the daily S values in July were remarkably low, with their daily average (~65 W m⁻²) only near a half of those in May and June (~120 W m⁻²), their contribution in July (97%) increased by 15% and 2% in comparison to May and June, respectively. In other words, the role of S as an energy source became increasingly important despite its gradually decreasing values. In contrast, the H values, together with its contribution, decreased continuously, with its monthly values (contributions) declining from 28 W m⁻² (18%) in May to only 2 W m⁻² (3%) in July.

Of the energy sinks in the SEB, L contributed the largest proportion (54%), complemented by the ΔQ and LE, which contributed 29% and 18%, respectively. There was a slight decrease in L from May to June (16 W m⁻²) but a subsequent remarkable reduction from June to July (58 W m⁻²). Similar to L, a striking declining trend was also found in LE, with its monthly magnitude decreasing from 40 W m⁻² in May to 16 W m⁻² in June and then further to only 4 W m⁻² in July. Comparatively, the energy change within the volume ΔQ increased continuously, with its monthly values increasing from 19 W m⁻² in May to 36 W m⁻² in June and increasing further to 45 W m⁻² in July. As a result of the decreasing L and LE but the increasing ΔQ trends, the contributions of L and LE both decreased, with their percentage proportions decreasing from 61% and 27% in May to 26% and 7% in July, respectively; whereas the contribution of ΔQ increased from the low proportions of <30% in May and June (13% and 28%, respectively) to a high contribution of 67% in July.

6.7. Mass Exchange at the Glacier Surface

Mass exchange at the glacier surface consists of sublimation/deposition, evaporation/condensation and melting. The half-hourly LE values show that deposition and condensation rarely occurred (not shown). Therefore, mass exchange at 6,523 m a.s.l. on the East Rongbuk mainly consisted of evaporation, sublimation and melt (Figures 6f–6h). Sublimation was persistent, while evaporation and glacier melting did not occur until late May. The daily sublimation values in May, June and July reached 1.2, 0.4, and 0.05 mm w.e., while the daily evaporation values in the above three months are 0, 0.1, and 0.08 mm w.e., respectively. The averaged daily glacier melt amounts in May, June, and July were 0.3, 8.4, and 8.2 mm w.e. Therefore, glacier melt is the dominative component of the surface ablation, followed by sublimation, while evaporation constituted only 1.2% of the glacier melt. Hence, evaporation only represents a minor part in the water cycle at this location and high altitude. Figure 6g also shows that before June, the sublimation rates were relatively high, but subsequently, they decreased until the end of the observational period. This can be partly attributed to the notable wind speed decrease. Evaporation and glacier melt, however, did not show similarly clear patterns. By summing up the daily evaporation, sublimation, and glacier melting, we obtained the daily ablation averages in May, June and July as 1.5, 8.9 and 8.3 mm w.e., respectively.

Sublimation was directly measured using a lysimeter by X. Yang (2010) near our AWS in 2008. The daily sublimation values observed over four days were 2.8 mm w.e. on 28 April, 1.9 mm w.e. on 30 April, 2.3 mm

Table 3
Sensitivity of Surface Energy Balance Components to Uncertainty in Parameter Values and Meteorological Variables

Variable/parameter	H %	LE %	S %	L %
$T + 0.2$ °C	+7.7	−4.5	–	–
$T − 0.2$ °C	−7.9	+7.8	–	–
$RH − 2\%$	–	+2.7	–	–
$RH + 2\%$	–	−2.7	–	–
$u − 0.3$	−3.5	−3.0	–	–
$u + 0.3$	+7.2	+4.5	–	–
$T + 1$ k	+36.9	−14.1	–	–
$T − 1$ k	−33.1	+12.7	–	–
$T_s − 1$ k	+37.7	−20.9	–	–
$T_s + 1$ k	−33.1	+20.0	–	–
$z − 0.5$ m	+7.7	+4.5	–	–
$z − 1$ m	+17.7	+11.8	–	–
$z + 0.5$ m	−1.5	−4.5	–	–
$z + 1$ m	−3.8	−12.3	–	–
$z_{om} = z_{ot} = z_{oq}$	44.6	38.6	–	–
$3 z_{om}$	+19.2	+15.9	–	–
$z_{om} + 1$ mm	+13.1	+10.5	–	–
$\alpha \pm 10\%$	–	–	±21%	–

w.e. on 1 May, and 0.66 mm w.e. on 2 May. The daily sublimation average in the above 4 days was 1.9 mm w.e., which is comparable to the values calculated in this study. Sublimation has also been reported on other glaciers. On the Xixibangma glacier, 130 km southwest of Rongbuk, the daily sublimation at a lower latitude of 5,900 m a.s.l. was 0.02 mm w.e. under nonmelting conditions (Aizen et al., 2002). On the Illimani glacier (Wagnon et al., 2003), daily sublimation was 1.2 mm w.e. from 22 to 25 in May and 0.7 mm w.e. from 14 May to 3 June; on the Antizana glacier, daily sublimation values of 0.5 and 0.8 mm w.e. were reported during 2 observational years (Favier et al., 2004); and on the Zongo glacier (Sicart, 2005), the averaged daily sublimation values was 1.1 mm w.e. from 23 July to 24 July. In addition, sublimation was also estimated by a distributed energy-balance model on the Juncal Norte glacier, Chile. It increased from 1.0 mm w.e. at 3,500 m a.s.l. to 1.5 mm w.e. at 5,500 m a.s.l. (Ayala et al., 2017). Overall, the daily sublimation rates obtained in our study are comparable to those previously reported.

6.8. Sensitivity of SEB Components to Uncertainty in Parameter Values and Meteorological Variables

Possible errors in the calculation of the SEB components need to be considered. Technical specifications provided by the sensor manufacturer (Table 1) suggest that uncertainties from the net radiation instrument can reach ±10%. Errors induced by the tilt of the tripod of AWS can be neglected since the AWS was regularly inspected and maintained. The CNR1 net radiometers used for radiation measurements in this study have a better performance than the manufacture's specifications under conditions of a measurement accuracy higher than 5% for daily averages (van den Broeke et al., 2004). Hence, the maximum error in the net radiation measurement should be smaller than 10% (approximately 4 W m^{-2}). Uncertainties in turbulent heat flux estimations could result from the accuracy of the meteorological sensors for the air temperature, moisture, and wind speed measurements (Table 1). Therefore, we perturbed the air temperature, relative humidity and wind speed within their accuracy ranges and recalculated the turbulent heat fluxes. Our results (Table 3) show that H and LE both varied by not more than 8% (1.1 W m^{-2} for H and 1.8 W m^{-2} for LE). This variation in magnitude is slightly lower than that of 10% on Laohugou No.12 glacier (Sun et al., 2012). The sensitivity of T and T_s to variations in ±1 K changed H and LE by approximately ±35% and ±16%, respectively. A change in the observation height inputted to SEB equation may have also introduced uncertainties in the turbulent heat calculation. When the observation height decreased/increased by 0.5 and 1.0 m, H and LE increased/decreased by 4.5%–17.7% and 1.5%–12.3%, respectively. The actual data of the observation height change induced by accumulation and ablation was not available because of the lack of precipitation measurements by precipitation gauges such as T-200B and SR50 sonic rangers. However, stake measurements starting on 10 June showed that snow surface increased its height by 30 cm during 10 June–22 June. Given that precipitation mainly takes place during the monsoonal period (from mid-June), snowfall before 10 June may be small and melting scarcely occurs due to the low temperature. Thus, 30 cm may largely represent the magnitude of observation height change over the whole observation period (1 May–22 July). Therefore, we estimated that the turbulent flux uncertainty introduced by observation height change was within the variation range mentioned above. Additionally, H and LE are also sensitive to variations in roughness lengths. As suggested by Favier et al. (2004) and Wagnon et al. (2003), when $z_{ot} = z_{oq} = z_{om}$ was adopted, H and LE increased by 44.6% (5.8 W m^{-2}) and 38.6% (8.5 W m^{-2}), respectively. When $3z_{om}$ and $z_{om}+1$ mm were inputted into the SEB equation, the increases in H and LE ranged from 10.5% to 19.2%. Changes of ±10% in albedo resulted in variations in S of ±21%. Moreover, the bulk aerodynamic method used for turbulent heat flux calculations could have introduced uncertainties. For example, W. Yang et al. (2011) found an averaged underestimation of less than 3 W m^{-2} for turbulent heat fluxes on Parlung No.4 glacier; Sun et al. (2014) stated the averaged underestimations

of H and LE on the Laohugou No.12 glacier were 3.4 and 1.2 W m^{-2}, respectively. For this study, however, the errors in the H and LE calculations introduced by the bulk aerodynamic method cannot be accurately evaluated since eddy-covariance observations were not simultaneously conducted in the field experiment. However, given that the three observational sites mentioned above are all located on TP, the averaged calculation errors on the East Rongbuk caused by it should be at the same level as on the Parlung No.4 and Laohugou No.12 glaciers, that is, approximately 3.3 W m^{-2} or even less. Finally, air temperatures in this study were measured in a naturally ventilated radiation shield, which could have led to high air temperature readings owing to potentially insufficient ventilation in the case of a low wind speed and a high shortwave radiation. We therefore estimated the air temperature measurement errors using the methodology suggested by Smeets (2006), and obtained a mean correction value of 0.12 °C, which was below the specification of the Vaisala temperature sensor (±0.2 °C). Thus, errors in turbulent heat flux calculation introduced by insufficient ventilation in air temperature measurement reached less than 8%, a value mentioned above when the turbulent heat fluxes were recalculated under the conditions of a changing air temperature within its accuracy range.

7. Discussion

7.1. The Significance of the SASM in Forcing SEB Variations

From the above analysis, it can be seen that there was a close phenomenological linkage between the glacio-meteorological conditions and the SASM. Therefore, we divided the entire observational period into three phases, namely P1, P2, and P3, based on the SASM index (downloaded from Asia-Pacific Data-Research center of the IPRC, http://apdrc.soest.hawaii.edu/projects/monsoon/realtime-monidx.html) (Figure 6i), and analyzed the SEB variation with the monsoon's advancement. From 1 to 28 May, the monsoon index (MI) was negative; thus, the days before 29 May are assigned to phase P1. This phase represents a time before monsoon onset. Since 29 May, however, MI shifted to be positive, indicating the onset of the SASM. We further calculated the average of daily MI values from 29 May to the ending day of 22 July, and took it as a threshold for classifying the residual days into P2 and P3. The days with daily MI smaller than the threshold are classified into phase P2 (29 May to 16 June), and the remaining days are assigned into P3. P2 represents the monsoon onset, whereas P3 represents an active period of a well-established monsoon. The three phases are shown in Figure 6i. Note that the P3 SASM start date of 16 June, that is, mid-June, is a frequently mentioned time in the above sections when meteorological variables changed dramatically. This implies a rapid response of the local meteorological conditions to SASM.

The observed meteorological conditions and the energy components in P1, P2, and P3 are summarized in Table 4. P1 was clear, dry, cold, and windy, having a daily wind speed average of 7.2 m s^{-1} and a daily air relative humidity average of 44%, and the sky was clear with a low average cloud fraction of 0.12. The glacier surface had a high albedo of 0.7 due to the seasonal snowpack. During P2, the wind speed was comparatively weak, and the air temperature and humidity were higher; the average wind speed decreased to 3.4 m s^{-1} and the cloud fraction increased to 0.17. The average daily air temperature and relative humidity increased by 5 °C and 15%, respectively, compared to P1. Meanwhile, the surface albedo was 0.03 lower (0.67), possibly due to snow metamorphosis as well as weak ablation. In comparison to P1 and P2, P3 was a cloudy, relatively humid, mild period, accompanied by weak winds and lower specific humidity and temperature differences between the atmosphere and surface. The average cloud coverage further increased to 0.38, and the average wind speed was low at 2.3 m s^{-1}. Additionally, the surface was frequently covered by fresh snow (Figure 4d), resulting in a high average surface albedo (0.76). Therefore, P3 was clearly strongly influenced by the SASM.

Both cloud cover and surface albedo can affect the radiation budget. In the northern Himalayas, clouds should have close linkage to the SASM, while surface albedo is mainly dependent on the amount of seasonal snow that has accumulated in winter, and during spring snowfall, as a result of the surface conditions during the melt seasons. The effect of clouds on the radiation budget is complex. On one hand, clouds reduce the incident solar radiation arriving at the glacier surface; on the other hand, they increase the downward longwave radiation, offsetting the energy loss to some extent. On the East Rongbuk glacier, P3 had the largest cloud cover, contributing less to the incident solar radiation than in P2 and P1 (Table 4). On average, $S\downarrow$ in P3 was 73 W m^{-2} lower than that in P2 and 81 W m^{-2} lower than that in P1. Meanwhile, from

P1 to P3, albedo increased. Although this potentially increases the magnitude of $S\uparrow$, $S\uparrow$ in P3 was reduced by 40 W m^{-2} mainly because of the lowest $S\downarrow$ value in P3, which eventually resulted in an S decrease of 42 W m^{-2} in P3 in comparison to P1. Therefore, when considering the effect on S, cloud cover was the dominant meteorological variable over albedo.

$L\downarrow$ showed large variations over the three observational phases. With the advancement of the monsoon, $L\downarrow$ in P3 was 97 W m^{-2} higher than that in P1 and 70 W m^{-2} higher than that in P2. In comparison, the variation in $L\uparrow$ was small, with $L\uparrow$ differences between P1, P2, and P3 less than 23 W m^{-2} (Table 3). Owing to the significant increase in $L\downarrow$, the net longwave radiation L increased significantly (53 W m^{-2} higher in P3 than in P2 and 56 W m^{-2} higher than in P1), and the magnitude of L increase was larger than the decrease of S, which eventually led to a slight R increase in P3 (4 W m^{-2} higher than in P2 and 16 W m^{-2} higher than in P1). This increased the melting energy since R provided the dominant energy supply for melting.

$S\downarrow$ and $L\downarrow$ are two crucial energy sources in the SEB and their changes are highly correlated with cloud cover. To quantitatively assess the influence of clouds on $S\downarrow$ and $L\downarrow$, we separated the measured $S\downarrow$ or $L\downarrow$ into two components: clear-sky and cloud-induced downward radiations. Many parameterization schemes have successfully estimated clear-sky $S\downarrow$ (Bird & Hulstrom, 1981; Conway et al., 2015; Essery & Marks, 2007; Iziomon & Mayer, 2002; Mölg et al., 2003; Pellicciotti et al., 2011) and clear-sky $L\downarrow$ (Conway et al., 2015; Culf & Gash, 1993; Juszak & Pellicciotti, 2013; Mölg et al., 2009; Niemelä et al., 2001a; Oerlemansutrecht, 2000; Sicart et al., 2006). The cloud-induced radiations can be obtained by subtracting the estimated clear-sky $L\downarrow$ and $S\downarrow$ from the measured counterparts. Niemelä et al. (2001a, 2001b) conducted comparisons of various $S\downarrow$ and $L\downarrow$ parameterization schemes and found that each scheme has its specific characteristic and utilization conditions. For example, the scheme for global and longwave incoming radiation developed by Konzelmann et al. (1994) can only be used when solar elevation is less than 66°. In this study, the scheme developed by Mölg et al. (2003) is adopted to estimate the clear-sky $S\downarrow$; the schemes initially developed by Brutsaert (1975) and further modified and used by Mölg et al. (2009) is used for clear-sky $L\downarrow$ estimation. The reason for choosing these two schemes is that they exhibited good performance in glacier environment.

The scheme of Mölg et al. (2003) for $S\downarrow$ estimation is a modified model of Hastenrath and Kruss (1988). Detailed information can be referenced to Mölg et al. (2003). Here we only show its main parameterization equation, which is written as $S\downarrow_{clear} = S_0 E_0 \cos\zeta_p [0.907/(\sin h)0.018]^{(T/\sin h)}$, where S_0 is solar constant, E_0 is the eccentricity correction factor, ζ_p is the zenith angle of the sun with respect to an arbitrarily oriented and inclined plane, h is the solar elevation, and T is the so-called Linke turbidity factor; these values can be obtained by other parameterization methods. The $L\downarrow$ parameterization used by Mölg et al. (2009) is written as $L\downarrow_{clear} = \varepsilon_{A\text{-clear}}\sigma T^4$, where clear-sky emissivity $\varepsilon_{A\text{-clear}}$ is expressed as $\varepsilon_{A\text{-clear}} = P1(e/T)^{1/P2}$ following Brutsaert (1975) who suggested P1 = 1.24 and P2 = 7 based on water-vapor pressure e (hpa) and air temperature T (K). Mölg et al. (2009) optimized P1 and P2 and found optimal values of P1 = 1.24 and P2 = 6 on the glacier surface they studied. The cloud-induced $S\downarrow$ and $L\downarrow$ are shown in Figure 7.

Clear difference existed between the modeled/measured $S\downarrow$ (Figure 7a) and $L\downarrow$(Figure 7b). Both differences were smallest in the pre-monsoon time but became largest in the active monsoon period, which obviously indicated the cloud's effect of decreasing $S\downarrow$ but increasing $L\downarrow$. In P1, clouds caused nearly equal effect on $S\downarrow$ and $L\downarrow$, inducing an $S\downarrow$ decrease of 78 W m^{-2} and an $L\downarrow$ increase of 80 W m^{-2}. Comparatively, clouds increased $L\downarrow$ more than they decreased $S\downarrow$ in P2. A decrease of 13 W m^{-2} in $S\downarrow$ and an increase of 87 m^{-2} in $L\downarrow$ were found. The largest changes in $S\downarrow$ and $L\downarrow$ were caused by the highest cloud cover in P3, with a decrease of 83 W m^{-2} in $S\downarrow$ and an increase of 143 W m^{-2} in $L\downarrow$, respectively. On average, clouds decreased $S\downarrow$ by 36 W m^{-2} and increased $L\downarrow$ by 109 W m^{-2} throughout the whole observational period. The variation amplitudes of $S\downarrow$ and $L\downarrow$ in the three periods all surpassed that of $L\uparrow$ (<23 W m^{-2}, mentioned above) and the maximum $S\uparrow$ change (the maximum $S\downarrow$ in P1 multiplied by albedo variation, that is, 403 W m$^{-2} \times$ (0.76–0.70) = 24 W m^{-2}), which were induced by variations in surface temperature and albedo, respectively. Therefore, clouds are the dominant variable affecting the radiation budget. They control the surface energy balance by increasing L↓ more than they decrease $S\downarrow$. In comparison, the effect of the albedo on the radiation change is not as influential as that of clouds since the variation in albedo was small (less than 0.1) at such a high altitude. Nevertheless, the role of albedo cannot be ignored. For example, if the albedo in P3 did not increase and remained at the same value of 0.70 in P1, $S\uparrow$ in P3 would be (322 × 0.70) 225 W m^{-2}, which is 15 W m^{-2} lower than the measured $S\uparrow$ of 240 W m^{-2}, which would further enlarge S and thus R.
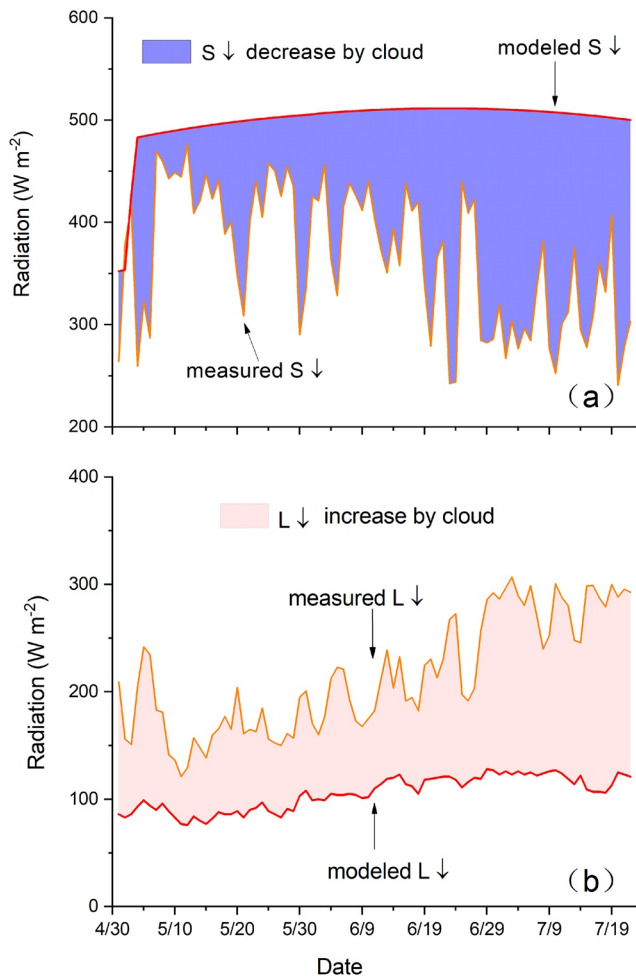
Figure 7. Comparison of $S\downarrow$ and $L\downarrow$ in clear-sky and all-sky conditions.

Table 4 also shows that the temperature and specific humidity differences between atmosphere and surface in P3 were much smaller than those in P1 and P2. This is also very likely associated with the presence of more clouds in P3. Owing to the insulating effect of clouds, clouds always tend to reduce surface cooling and near-surface gradients. Moreover, the monsoon clouds in P3 were more closely associated with the more frequent precipitation in the monsoonal period, which will increase the moisture content in the air and thus decrease moisture gradients between atmosphere and the saturated glacier surface.

The energy change of glacier ΔQ in the monsoon active period of P3 was approximately 11 W m^{-2} larger than that in P2 and 24 W m^{-2} higher than that in P1. The largest H values appeared in P1, which is the result of the rare combination of windy and clear-sky conditions during P1. The differences in LE between the three observational phases (e.g., 19 W m^{-2} between P1 and P2 and 15 W m^{-2} between P2 and P3) were more evident than those in H (e.g., 17 W m^{-2} between P1 and P2 and 8 W m^{-2} between P2 and P3) and those in R (13 W m^{-2} between P1 and P2 and 4 W m^{-2} in P2 and P3). Therefore, the variability in LE provided an important cause of variations in ΔQ and surface melting, despite its relatively small absolute contribution. In this study, glacier melting was suppressed by the upward LE because of energy consumed by sublimation and evaporation, while on some maritime glaciers such as Parlung No.4 glacier in summertime, a downward directed LE causes condensation, thereby releasing energy and enhancing surface melting. Sublimation plays a crucial role in the mass- and energy-balance of TP glaciers. It is generally regarded as a favorable factor for the existence of high-altitude glaciers as it limits the energy supply for melting (Wagnon, Ribstein, Francou, & Pouyaud, 1999). As the latent heat of sublimation (2.834×10^6 J Kg^{-1}) is nearly 10 times the latent heat of fusion (3.34×10^5 J kg^{-1}), the energy consumed by sublimation is nearly 10 times larger than that used for an equal amount of melting. Therefore, sublimation can significantly decrease the energy supply for glacier melting. The averages of the relative contribution of LE to surface melting in P1, P2, and P3 was -124%, -17%, and -4%, respectively. High wind speeds and dry atmospheric conditions in P1 produced more turbulent latent heat, favoring sublimation but suppressing glacier melting.

The daily cycles of the meteorological variables as well as the daily evolution of the S, L, H, LE, and ΔQ are shown in Figure 8. Overall, all of the meteorological variables together with the SEB components followed nearly similar diurnal variation patterns in the three observational phases despite distinctive differences in their magnitudes. The wind speed u, air temperatures T, surface temperature T_s, and specific humidity q and q_s all increased from the morning (about 10:00), peaked in the early afternoon (around 15:00) and then gradually decreased till the next morning. The magnitude of diurnal variation u decreased with the observation phases, ranging from 3.4 m s^{-1} in P1 to 2.7 m s^{-1} and 2.0 m s^{-1} in P2 and P3, respectively. The diurnal cycles of T and T_s showed that at night, the difference between them was large, and there was a temperature inversion, while in daytime, the difference decreased, and the temperature inversion disappeared, especially from approximately 12:00 to 18:00. Moreover, the duration time of temperature inversion decreased with the advancement of the monsoon, from 18.2 h in P1 to 16 h in P3. Glacier melting mainly occurred in P3, particularly at noon, as T_s reached 0 °C more frequently than in P1 and P2. Contrary to the diurnal variation in temperature difference between T and T_s, the moisture difference between air and surface was small at night but large during the daytime.

S showed pronounced diurnal cycles in P1, P2, and P3. It started to increase in morning, peaked at noon and then decreased to null at night, with diurnal variation magnitudes in the three phases of 386, 410, and

Table 4
Averages of the Meteorological Elements and Energy Components During Three Different Periods (P1, P2, and P3) With the Advancement of the South Asian Monsoon

Elements	P1 (1 May–28 May)	P2 (29 May–16 June)	P3 (17 June–22 July)	Whole period
T (°C)	−11.6	−6.6	−3.7	−7.0
ΔT (°C)[a]	4.2	3.5	1.9	3.1
RH (%)	44	60	71	60
Δq (g kg^{-1})[b]	−1.4	−1.4	−0.6	−1.0
Wind speed (m s^{-1})[c]	7.2	3.4	2.3	4.2
Down-glacier wind frequency[d]	17	27	36	27
Up-glacier wind frequency[e]	51	23	16	29
Cloud coverage	0.12	0.17	0.38	0.25
Surface albedo	0.70	0.67	0.76	0.72
$S\downarrow$ (W m^{-2})	403	395	322	366
$S\uparrow$ (W m^{-2})	−281	−264	−240	−259
$L\downarrow$ (W m^{-2})	160	186	257	208
$L\uparrow$ (W m^{-2})	−251	−274	−292	−274
S (W m^{-2})	122	131	82	107
L (W m^{-2})	−91	−88	−35	−66
R (W m^{-2})	30	43	47	40
H (W m^{-2})	28	11	3	13
LE (W m^{-2})	−41	−22	−7	−22
G (W m^{-2})	0	0	−0	0
ΔQ_m (W m^{-2})	0	24	34	20
ΔQ_s (W m^{-2})	19	8	7	11

[a]Temperature difference ($T-T_s$). [b]Specific humidity difference ($q-q_s$). [c]Wind speed at 2.5 m. [d]The accumulative wind frequency (%) when 90° < wind direction ≤ 180°. [e]The accumulative wind frequency (%) when 270° ≤ wind direction < 360°.

277 W m^{-2}, respectively. However, compared to S, L varied with a smaller diurnal variation magnitude (42–61 W m^{-2}). It remained nearly constant during the night but produced a lower value in the daytime. From 09:00 to 12:00, L decreased but increased afterward until 18:00. This was mainly caused by the higher $L\uparrow$ in the daytime resulting from the increased T_s. The turbulent heat fluxes, H and LE, had identical variation trends for all the three periods. The magnitude of H was larger than that of LE at nighttime but lower in the daytime, resulting in downward $LE + H$ at night but upward in the daytime. At night, the colder surface cooled the air, and the atmospheric stratification was stable. H represents an energy sources because of the temperature gradient between air and surface and was >0. Throughout the daytime, however, the glacier surface was rapidly warmed by $S\downarrow$, decreasing the temperature difference between air and surface and finally leading to a higher surface temperature than the air temperature, which resulted in $H < 0$, and its direction shift from facing downward to upward. Daytime LE was persistently larger than that at night because of the higher moisture differences in the daytime than at night. During P1 and P2, $LE < 0$ and glacier surface sublimated over the entire day. In P3, however, the direction of LE in nighttime was downward, indicating the occurrence of desublimation at nighttime. H and LE were largest in P1, which can be explained by the large wind speeds and the clear-sky conditions.

The diurnal variation in R is the result of changes in S and L. In P1, R in daytime was larger than that in P3, but smaller overnight. This indicated that the glacier surface was warmed in the daytime but cooled during the night with a stronger intensity in P1 than in P3. This was more closely related to the lower cloudiness seen in P1 than that in P3 (see the discussion above). The energy change within the volume ΔQ, that is,
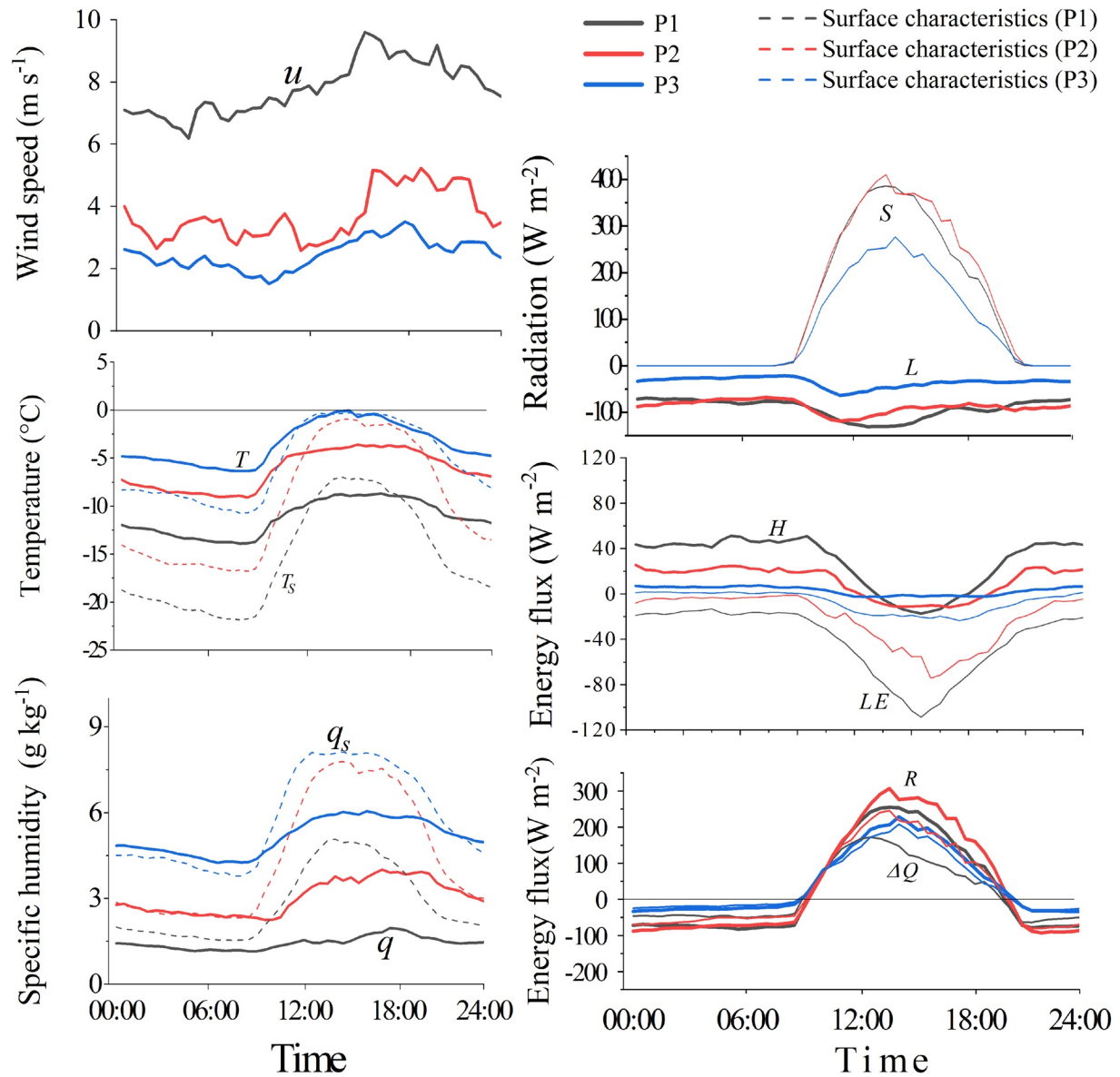
Figure 8. The average daily cycle of meteorological and SEB variables during P1(gray lines), P2 (red lines), and P3 (blue lines). Dotted lines are the surface characteristics of surface temperature (T_s) and surface specific humidity (q_s). Thick lines are wind speed (u), air temperature (T), air specific humidity (q), net longwave radiation (L), sensible heat (H) and net all-wave radiation (R). Thin lines represent the net shortwave radiation (S), latent heat (LE), and the energy change within the glacier volume (ΔQ). SEB, surface energy balance.

$\Delta Q_s + \Delta Q_m$, followed the cycle of R. The negative ΔQ in night indicated the energy release from the glacier, and the temperature of the glacier volume was lower than that in the daytime, whereas the positive ΔQ in the daytime was first used to warm the glacier volume and then melt the glacier when the glacier surface was warmed enough to raise the surface temperature to 0 °C.

7.2. SEB Comparison to Other Glaciers on TP

SEB studies have also been conducted on many other glaciers on TP. Therefore, we collect SEB data previously reported on the TP to find possible differences between them. Because there is widespread concern about relationship between glacier melting and climate, only the SEB components in the ablation zone over ablation season (May–October) were chosen (Table 5), which was guaranteed by only choosing the studies

Table 5
The Surface Energy Components (W m^{-2} [%]) Reported on Different Types of Glaciers on Tibetan Plateau During Ablation Season

Glacier type[a]	Glacier name	Lat. °N	Long. °E	Elevation (m a.s.l.)	ELA	Period	R	H	LE	G	ΔQ	Source
Highly continental	Chongce ice cap	35.2	81.01	5,850	5,930[b]	Jul–Aug 1987	36 (67)	17 (33)	−39 (74)	–	−14 (26)	Takahashi et al. ([1989](#))
	Qiangtang No. 1	33.3	88.7	5,882	5,900[c]	Jun–Sep 2012–2016	27 (75)	9 (25)	−18 (51)	0 (1)	−17 (49)	S. Li et al. ([2018](#))
Subcontinental	Zhadang	30.4	90.6	5,655	5,810[d]	May–Sep 2011	39 (83)	8 (17)	−11 (23)	−11 (23)	−25 (53)	Zhu et al. ([2015](#))
	Laohugou No.12	39.48	96.35	4,550	4,830[e]	Jun–Sep 2011	81 (93)	6.5 (7)	−12.8 (15)	0	−74.7 (85)	Sun et al. ([2014](#))
	Qiyi	39.5	97.7	4,473	4,773[f]	Jul–Oct 2007	63 (82)	14 (18)	−6 (8)	−16 (20)	−56 (72)	Jiang et al. ([2010](#))
	Keqicar Baxi	41.8	80.5	4,200	4,631[g]	Jun–Sep 2005	63 (82)	14 (19)	−23 (30)	–	−54 (70)	J. Li et al. ([2007](#))
	Xixiabangma	28.5	85.7	5,700	5,900[h]	Aug 23–Sep 29, 1991	28 (86)	5 (14)	−19 (57)	–	−14 (43)	Aizen et al. ([2002](#))
Maritime	Parlung No. 4	29.2	96.8	4,800	5,397[i]	May–Sep 2009	149 (84)	28 (16)	−1 (1)	−1 (1)	−175 (99)	W. Yang, Guo, et al. ([2011](#))
	Parlung No. 4	29.2	96.8	5,202	5,397[i]	May–Sep 2011	84 (88)	12 (13)	−11 (12)	−12 (13)	−73 (76)	Zhu et al. ([2015](#))

[a]Classified according to Shi ([2002](#)). [b]Ageta and Higuchi ([1984](#)). [c]S. L et al. ([2018](#)). [d]Yu et al. ([2013](#)). [e]Kang and Ding ([1981](#)). [f]N. Wang et al. ([2010](#)). [g]Y. Zhang et al. ([2006](#)). [h]Aizen et al. ([2002](#)). [i]Yao et al. ([2010](#)).

conducted at altitudes lower than the ELA. It must be noted that the conclusion drawn here may be altered by different methods for turbulent heat flux calculations and different measurement accuracies of the meteorological sensors, as well as different meteorological conditions (such as clouds) in different observational years. This comparison aims to give a possible schematic description of the glacier SEB characteristics spatially throughout the whole TP.

From the perspective of the energy input, *R* constitutes the largest energy source and supplies most of the energy input on all studied Tibetan glaciers, followed by *H*. On most subcontinental and maritime glaciers, net radiation provides 75%–80% of the energy. Comparatively, on the highly continental glaciers, the percentage contribution of *R* appears to decline (around 70%). For this experiment conducted on the East Rongbuk glacier, although it is located in the accumulation zone, the contribution of *R* reached 75%, and a moderate level among the glaciers is examined here. As *R* and *H* consist of the only two energy sources on the majority of Tibetan glaciers, compared to *R*, the percentage proportions of *H* were low on most maritime/subcontinental glaciers, ranging from 7% to 19%. However, on the highly continental glaciers, the contributions of *H* appeared larger (>20%). Therefore, on the TP, as glaciers become more continental, the percentage contribution of *R* (*H*) became lower (higher). This can be explained by the different latitudes that determine solar angle and sunshine duration. Compared to the maritime/subcontinental glaciers, the highly continental glaciers on TP are generally located at higher latitudes, receive less solar radiations and thus have smaller *R* values in comparison to maritime/subcontinental glaciers.

From the perspective of energy sinks, on most of the subcontinental and maritime glaciers, energy fluxes were primarily consumed by surface melting, with its percentage contribution mostly ranging from 50% to 70%; contributions of *LE* were generally small, mostly ranging from 10% to 30% (except for 57% on the Xixiabangma). Comparatively, on the highly continental glaciers, the energy sink was dominated by surface sublimation and evaporation and contributed >50% of the energy sink total. On the TP, as most of the moisture is transported from the southeast by the SASM intruding (Feng & Zhou, [2012](#)), there is a clear southeast-northwest precipitation gradient, which ranges from over 6,000 mm yr^{-1} in the southeast Himalayan foothills to less than 50 mm yr^{-1} in the inland Tarim basin on the northwest TP (Maussion et al., [2014](#)). The

above pattern in the energy sinks of the Tibetan glaciers agrees with Rupper and Roe (2008), who pointed out that ablation at the equilibrium line altitude was dominated by sublimation (LE associated) under low-precipitation conditions but was controlled by melting in the case of high precipitation and appeared to agree well with the findings of Fujita and Nuimura (2011), who stated that there was an accelerated mass loss (dominated by melting and runoff) in humid climate regimes but a reduced mass-loss rate in arid climatic conditions (probably because most energy was consumed by sublimation rather than melting). The two highly continental glaciers included in our comparison were both located in the arid inland TP, where the local circulations seemed to control the local cold-dry meteorological conditions, especially the moisture regime (Mölg et al., 2012). Therefore they are assumed to be less sensitive to the SASM (Tian et al., 2001) and thus likely experience lower precipitation amounts during the onset of the intensified SASM (June–September) in comparison to the maritime/subcontinental glaciers located in the periphery of TP.

Overall, the above analysis shows that there appeared to be a clear difference in energy supply/consumption between the subcontinental/maritime and highly continental glaciers. This implies that there was a spatial variability in glacial sensitivity to climate change on different glaciers. The SASM exerts effects on SEB not only directly by modulating the moisture conditions, but also indirectly by altering the energy supply through the cloud cover. Nevertheless, the available energy experiments listed in Table 5 are assumed to represent the mean SEB statuses and not the interannual variation in climatic conditions. Therefore, spatially quantitative determination of the relationship between melting energy and climatic conditions requires future work, including synchronous collection of measurement using the same experimental procedures on different types of glaciers.

8. Conclusions

We calculated the SEB of the East Rongbuk glacier located in the northern slope of Mt. Qomolangma using the in situ meteorological data at 6,523 m a.s.l. obtained from May 1 to July 22, 2005. In the summertime, S and H represented energy sources, with average values of 103 and 12 W m^{-2}, respectively. G was an energy source, but its value was not significantly different from zero (0.1 W m^{-2}), and therefore, it was considered negligible. S was the dominant energy source with an average contribution of 89%, while H provided only near 11%. L and LE represented heat sinks, with their respective averages being -62 and -20 W m^{-2}. A close phenomenological link exists between glacio-meteorological conditions and the SASM. Cloud was the primary variable affecting the SEB. During the monsoon time, the increased cloud covers increased $L\downarrow$ more than it decreased $S\downarrow$, which eventually led to increase in R. Meanwhile, wind speeds decreased significantly, resulting in remarked decreases in both H and LE. Seasonal changes in melting energy were mainly driven by LE. During the nonmonsoonal period, the melting energy was small, mainly due to the large energy losses in longwave radiation and sublimation. Finally, a preliminary analysis of the spatial characteristics of glacier energy fluxes on the whole TP described possible energy balance patterns between maritime/subcontinental and highly continental glaciers. Net radiation provides the largest energy source and supplies most of the energy input for Tibetan glaciers, followed by the sensible heat flux H. There is a shift of energy sinks from sublimation and evaporation on the highly continental glaciers to melting on the maritime/subcontinental glaciers. On the highly continental glaciers, the energy sink was dominated by sublimation and evaporation, while on the maritime/subcontinental glaciers, the energy sink was dominant by glacier melting. This reveals a spatial variability in glacial sensitivity to different climatic conditions on the TP.

This study provides a new understanding of the interaction between ice/snow and atmosphere on monsoon-influenced Himalayan glacier. More long-term SEB researches on different types of glaciers on the TP under various climate backgrounds, as well as their relationship with large-scale atmospheric circulations, are needed to further improve the modeling of glacier response to climate change.

Data Availability Statement

All data sets used in this study are uploaded to the following website https://data.tpdc.ac.cn/en/disallow/0864bef1-b59a-4019-b2e7-30676e977e2b/. The south Asian monsoon index is downloaded from Asia-Pacific Data-Research center of the IPRC (http://apdrc.soest.hawaii.edu/projects/monsoon/real-time-monidx.html).

References

Agarwal, V., Bolch, T., Syed, T. H., Pieczonka, T., Strozzi, T., & Nagaich, R. (2017). Area and mass changes of Siachen Glacier (East Karakoram). *Journal of Glaciology*, *63*(237), 148–163. https://doi.org/10.1017/jog.2016.127

Ageta, Y., & Higuchi, K. (1984). Estimation of mass balance components of a summer-accumulation type glacier in the Nepal Himalaya. *Geografiska Annaler. Series A, Physical Geography*, *66*(3), 249–255. https://doi.org/10.2307/520698

Aizen, V. B., Aizen, E. M., & Nikitin, S. A. (2002). Glacier regime on the northern slope of the Himalaya (Xixibangma glaciers). *Quaternary International*, *97–98*, 27–39. https://doi.org/10.1016/s1040-6182(02)00049-6

Andreas, E. L. (1987). A theory for the scalar roughness and the scalar transfer coefficients over snow and sea ice. *Boundary-Layer Meteorology*, *38*(1–2), 159–184. https://doi.org/10.1007/bf00121562

Andreas, E. L. (2002). Parameterizing scalar transfer over snow and ice: A review. *Journal of Hydrometeorology*, *3*(4). https://doi.org/10.1175/1525-7541(2002)003<0417:pstosa>2.0.co;2

Arck, M., & Scherer, D. (2002). Problems in the determination of sensible heat flux over snow. *Geografiska Annaler*, *84*(3–4), 157–169. https://doi.org/10.1111/j.0435-3676.2002.00170.x

Ayala, A., Pellicciotti, F., Peleg, N., & Burlando, P. (2017). Melt and surface sublimation across a glacier in a dry environment: Distributed energy-balance modelling of Juncal Norte Glacier, Chile. *Journal of Glaciology*, *63*(241), 803–822. https://doi.org/10.1017/jog.2017.46

Azam, M. F., Wagnon, P., Berthier, E., Vincent, C., Fujita, K., & Kargel, J. S. (2018). Review of the status and mass changes of Himalayan-Karakoram glaciers. *Journal of Glaciology*, *64*(243), 61–74. https://doi.org/10.1017/jog.2017.86

Barnett, T. P., Adam, J. C., & Lettenmaier, D. P. (2005). Potential impacts of a warming climate on water availability in snow-dominated regions. *Nature*, *438*(7066), 303–309. https://doi.org/10.1038/nature04141

Bintanja, R., & Reijmer, C. H. (2001). Meteorological conditions over Antarctic blue-ice areas and their influence on the local surface mass balance. *Journal of Glaciology*, *47*(156), 60–66. https://doi.org/10.3189/172756501781832557

Bird, R. E., & Hulstrom, R. L. (1981). A Simplified clear sky model for direct and diffuse insolation on horizontal surfaces (Technical Report Rep. SERI/TR-642-761): Solar Energy Research Institute. https://doi.org/10.2172/6510849

Bolch, T., Kulkarni, A., Kääb, A., Huggel, C., Paul, F., Cogley, J. G., et al. (2012). The state and fate of Himalayan glaciers. *Science*, *336*(6079), 310–314. https://doi.org/10.1126/science.1215828

Brock, B. W., Mihalcea, C., Kirkbride, M. P., Diolaiuti, G., Cutler, M. E. J., & Smiraglia, C. (2010). Meteorology and surface energy fluxes in the 2005–2007 ablation seasons at the Miage debris-covered glacier, Mont Blanc Massif, Italian Alps. *Journal of Geophysical Research*, *115*(D9). https://doi.org/10.1029/2009jd013224

Brock, B. W., Rivera, A., Casassa, G., & Acuña, F. C. (2007). The surface energy balance of an active ice-covered volcano: Villarrica Volcano, southern Chile. *Annals of Glaciology*, *45*(1), 104–114. https://doi.org/10.3189/172756407782282372

Brock, B. W., Willis, I. C., & Sharp, M. J. (2006). Measurement and parameterization of aerodynamic roughness length variations at Haut Glacier d'Arolla, Switzerland. *Journal of Glaciology*, *52*(177), 281–297. https://doi.org/10.3189/172756506781828746

Brutsaert, W. (1975). On a derivable formula for long-wave radiation from clear skies. *Water Resources Research*, *11*(5), 742–744. https://doi.org/10.1029/wr011i005p00742

Brutsaert, W. (1982). *Evaporation into the atmosphere: Theory, history and applications* (p. 299). Springer Netherlands.

Cannon, F., Carvalho, L. M. V., Jones, C., & Bookhagen, B. (2015). Multi-annual variations in winter westerly disturbance activity affecting the Himalaya. *Climate Dynamics*, *44*(1), 441–455. https://doi.org/10.1007/s00382-014-2248-8

Carenzo, M., Pellicciotti, F., Mabillard, J., Reid, T., & Brock, B. W. (2016). An enhanced temperature index model for debris-covered glaciers accounting for thickness effect. *Advances in Water Resources*, *94*, 457–469. https://doi.org/10.1016/j.advwatres.2016.05.001

Conway, J. P., Cullen, N. J., Spronken-Smith, R. A., & Fitzsimons, S. J. (2015). All-sky radiation over a glacier surface in the Southern Alps of New Zealand: Characterizing cloud effects on incoming shortwave, longwave and net radiation. *International Journal of Climatology*, *35*(5), 699–713. https://doi.org/10.1002/joc.4014

Culf, A. D., & Gash, J. H. C. (1993). Longwave radiation from clear skies in Niger: A comparison of observations with simple formulas. *Journal of Applied Meteorology*, *32*(3), 539–547. https://doi.org/10.1175/1520-0450(1993)032<0539:lrfcsi>2.0.co;2

Dahe, Q., Shugui, H., Dongqi, Z., Jiawen, R., Shichang, K., Mayewski, P. A., & Wake, C. P. (2017). Preliminary results from the chemical records of an 80.4 m ice core recovered from East Rongbuk Glacier, Qomolangma (Mount Everest), Himalaya. *Annals of Glaciology*, *35*, 278–284. https://doi.org/10.3189/172756402781816799

Daniel Moore, R. (1983). On the use of bulk aerodynamic formulae over melting snow. *Hydrology Research*, *14*(4), 193–206. https://doi.org/10.2166/nh.1983.0016

Denby, B., & Greuell, W. (2000). The use of bulk and profile methods for determining surface heat fluxes in the presence of glacier winds. *Journal of Glaciology*, *46*(154), 445–452. https://doi.org/10.3189/172756500781833124

Ding, M., Yang, D., Broeke, M. R., Allison, I., Xiao, C., Qin, D., & Huai, B. (2020). The surface energy balance at Panda 1 Station, Princess Elizabeth Land: A typical katabatic wind region in East Antarctica. *Journal of Geophysical Research: Atmospheres*, *125*(3), e2019JD030378. https://doi.org/10.1029/2019jd030378

Essery, R., & Marks, D. (2007). Scaling and parametrization of clear-sky solar radiation over complex topography. *Journal of Geophysical Research*, *112*(D10). https://doi.org/10.1029/2006jd007650

Favier, V., Wagnon, P., Chazarin, J.-P., Maisincho, L., & Coudrain, A. (2004). One-year measurements of surface heat budget on the ablation zone of Antizana Glacier 15, Ecuadorian Andes. *Journal of Geophysical Research*, *109*(D18). https://doi.org/10.1029/2003jd004359

Feng, L., & Zhou, T. (2012). Water vapor transport for summer precipitation over the Tibetan Plateau: Multidata set analysis. *Journal of Geophysical Research*, *117*(D20). https://doi.org/10.1029/2011jd017012

Francou, B., Ribstein, P., Wagnon, P., Ramirez, E., & Pouyaud, B. (2005). Glaciers of the tropical Andes: Indicators of global climate variability. In *Global change and mountain regions* (pp. 197–204): Springer.

Fujita, K., & Nuimura, T. (2011). Spatially heterogeneous wastage of Himalayan glaciers. *Proceedings of the National Academy of Sciences*, *108*(34), 14011–14014. https://doi.org/10.1073/pnas.1106242108

Fujita, K., Seko, K., Ageta, Y., Jianchen, P., & Tandong, Y. (2017). Superimposed ice in glacier mass balance on the Tibetan Plateau. *Journal of Glaciology*, *42*(142), 454–460. https://doi.org/10.3189/S002214300000344010.1017/s0022143000003440

Greuell, W., & Smeets, P. (2001). Variations with elevation in the surface energy balance on the Pasterze (Austria). *Journal of Geophysical Research*, *106*(D23), 31717–31727. https://doi.org/10.1029/2001jd900127

Guo, X., Yang, K., Zhao, L., Yang, W., Li, S., Zhu, M., et al. (2011). Critical evaluation of scalar roughness length parametrizations over a melting valley glacier. *Boundary-Layer Meteorology*, *139*(2), 307–332. https://doi.org/10.1007/s10546-010-9586-9

Hastenrath, S., & Kruss, P. D. (1988). The role of radiation geometry in the climate response of mount kenya's glaciers, part 2: Sloping versus horizontal surfaces. *Journal of Climatology*, *8*(6), 629–639. https://doi.org/10.1002/joc.3370080606

Hou, S., Qin, D., Wake, C. P., Mayewski, P. A, Ren, J., & Yang, Q. (2000). Climatological significance of an ice core net-accumulation record at Mt. Qomolangma (Everest). *Chinese Science Bulletin*, *45*(1001–6538), 259. https://doi.org/10.1007/bf02884687

Hou, S., Qin, D., Yao, T., Zhang, D., & Chen, T. (2002). Recent change of the ice core accumulation rates on the Qinghai-Tibetan Plateau. *Chinese Science Bulletin*, *47*(1001–6538), 1746. https://doi.org/10.1007/bf03183321

Iziomon, M. G., & Mayer, H. (2002). Assessment of some global solar radiation parameterizations. *Journal of Atmospheric and Solar-Terrestrial Physics*, *64*(15), 1631–1643. https://doi.org/10.1016/s1364-6826(02)00131-1

Jiang, X., Wang, N., & Yang, S. (2010). The surface energy balance on the Qiyi Glacier in Qilian Mountains during the ablation period (in Chinese). *Journal of Glaciology and Geocryology*, *32*(4), 686–695.

JianZhong Xu, S. K., ShuGui, H., QiangGong, Z., Jie, H., CunDe, X., JiaWen, R., & DaHe, Q, (2016). Characterization of contemporary aeolian dust deposition on mountain glaciers of western China. *Sciences in Cold and Arid Regions*, *8*(1), 9–21. https://doi.org/10.3724/sp.j.1226.2016.00009

Juszak, I., & Pellicciotti, F. (2013). A comparison of parameterizations of incoming longwave radiation over melting glaciers: Model robustness and seasonal variability. *Journal of Geophysical Research: Atmospheres*, *118*(8), 3066–3084. https://doi.org/10.1002/jgrd.50277

Kang, X., & Ding, L. (1981). Relation of mass balance, ELA and climate in Tianshan Mountain and Qilian Mountain. *Journal of Glaciology and Geocryology*, *31*(1), 53–56.[in Chinese].

Kayastha, R. B., Takeuchi, Y., Nakawo, M., & Ageta, Y. (2000). Practical prediction of ice melting beneath various thickness of debris cover on Khumbu Glacier, Nepal, using a positive degree-day factor (Vol. 264, pp. 71–81). IAHS Publication.

King, J. C., & Anderson, P. S. (1994). Heat and water vapor fluxes and scalar roughness over an Antarctic ice shelf. *Boundary-Layer Meteorology*, *69*(1–2), 101–121. https://doi.org/10.1007/bf00713297

Konzelmann, T., Vandewal, R., Greuell, W., Bintanja, R., Henneken, E., & Abeouchi, A. (1994). Parameterization of global and longwave incoming radiation for the Greenland Ice Sheet. *Global and Planetary Change*, *9*(1), 143–164. https://doi.org/10.1016/0921-8181(94)90013-2

Li, J., Liu, S., & Zhang, Y. (2007). Snow surface energy balance over the ablation period on the Keqicar Baxi Glacier in the Tienshan Mountains (in Chinese). *Journal of Glaciology and Geocryology*, *29*(3), 366–373.

Li, S., Yao, T., Yang, W., Yu, W., & Zhu, M. (2018). Glacier Energy and Mass Balance in the Inland Tibetan Plateau: Seasonal and Interannual Variability in Relation to Atmospheric Changes. *Journal of Geophysical Research: Atmospheres*, *123*(12), 6390–6409. https://doi.org/10.1029/2017JD028120

Liu, W., Ren, J., Qin, X., Liu, J., Liu, Q., Cui, X., & Wang, Y. (2010). Hydrological characteristics of the Rongbuk Glacier catchment in Mt. Qomolangma region in the central Himalayas, China. *Journal of Mountain Science*, *7*(2), 146–156. https://doi.org/10.1007/s11629-010-1069-4

Maussion, F., Scherer, D., Mölg, T., Collier, E., Curio, J., & Finkelnburg, R. (2014). Precipitation seasonality and variability over the Tibetan Plateau as resolved by the high Asia reanalysis. *Journal of Climate*, *27*(5), 1910–1927. https://doi.org/10.1175/jcli-d-13-00282.1

Mi, D., & Xie, Z. (2002). *Glacier inventory of China: The Ganga drainage basin and Indus river drainage basin*. Xi'an Cartographic publishing House.

Mölg, T., Cullen, N. J., & Kaser, G. (2009). Solar radiation, cloudiness and longwave radiation over low-latitude glaciers: Implications for mass-balance modelling. *Journal of Glaciology*, *55*(190), 292–302. https://doi.org/10.3189/002214309788608822

Mölg, T., Georges, C., & Kaser, G. (2003). The contribution of increased incoming shortwave radiation to the retreat of the Rwenzori Glaciers, East Africa, during the 20th century. *International Journal of Climatology*, *23*(3), 291–303. https://doi.org/10.1002/joc.877

Mölg, T., & Hardy, D. R. (2004). Ablation and associated energy balance of a horizontal glacier surface on Kilimanjaro. *Journal of Geophysical Research*, *109*, D16104. https://doi.org/10.1029/2003jd004338

Mölg, T., Maussion, F., Yang, W., & Scherer, D. (2012). The footprint of Asian monsoon dynamics in the mass and energy balance of a Tibetan glacier. *The Cryosphere*, *6*(6), 1445–1461. https://doi.org/10.5194/tc-6-1445-2012

Morris, E. M. (1989). Turbulent transfer over snow and ice. *Journal of Hydrology*, *105*(3), 205–223. https://doi.org/10.1016/0022-1694(89)90105-4

Munro, D. S. (1989). Surface roughness and bulk heat transfer on a glacier: Comparison with eddy correlation. *Journal of Glaciology*, *35*, 343–348. https://doi.org/10.1017/s0022143000009266

Niemelä, S., Räisänen, P., & Savijärvi, H. (2001a). Comparison of surface radiative flux parameterizations. *Atmospheric Research*, *58*(1), 1–18. https://doi.org/10.1016/s0169-8095(01)00084-9

Niemelä, S., Räisänen, P., & Savijärvi, H. (2001b). Comparison of surface radiative flux parameterizations. *Atmospheric Research*, *58*(2), 141–154. https://doi.org/10.1016/s0169-8095(01)00085-0

Obleitner, F., & De Wolde, J. (1999). On intercomparison of instruments used within the Vatnajökull Glacio-meteorological experiment. *Boundary-Layer Meteorology*, *92*(1), 25–35. https://doi.org/10.1023/a:1002074627334

Oerlemans, J. (2000). Analysis of a 3 year meteorological record from the ablation zone of Morteratschgletscher, Switzerland: Energy and mass balance. *Journal of Glaciology*, *46*(155), 571–579. https://doi.org/10.3189/172756500781832657

Oke, T. R. (1987). *Boundary layer climates* (2nd ed., p. 435). Routledge.

Paterson, W. S. B. (1994). *The physics of glacier* (3rd ed.): Tarrytown.

Pellicciotti, F., Raschle, T., Huerlimann, T., Carenzo, M., & Burlando, P. (2011). Transmission of solar radiation through clouds on melting glaciers: A comparison of parameterizations and their impact on melt modelling. *Journal of Glaciology*, *57*(202), 367–381. https://doi.org/10.3189/002214311796406013

Pellicciotti, F., Stephan, C., Miles, E., Herreid, S., Immerzeel, W. W., & Bolch, T. (2015). Mass-balance changes of the debris-covered glaciers in the Langtang Himal, Nepal, from 1974 to 1999. *Journal of Glaciology*, *61*(226), 373–386. https://doi.org/10.3189/2015jog13j237

Qin, J., Yang, K., Liang, S., & Guo, X. (2009). The altitudinal dependence of recent rapid warming over the Tibetan Plateau. *Climatic Change*, *97*(1–2), 321–327. https://doi.org/10.1007/s10584-009-9733-9

Reid, T. D., & Brock, B. W. (2010). An energy-balance model for debris-covered glaciers including heat conduction through the debris layer. *Journal of Glaciology*, *56*(199), 903–916. https://doi.org/10.3189/002214310794457218

Ren, J., Qin, D., Kang, S., Hou, S., Pu, J., & Jing, Z. (2004). Glacier variations and climate warming and drying in the central Himalayas. *Chinese Science Bulletin*, *49*(1), 65. https://doi.org/10.1360/03wd014810.1007/bf02901744

Rupper, S., & Roe, G. (2008). Glacier changes and regional climate: A mass and energy balance approach. *Journal of Climate*, *21*(20), 5384–5401. https://doi.org/10.1175/2008jcli2219.1

Scherler, D., Bookhagen, B., & Strecker, M. R. (2011). Spatially variable response of Himalayan glaciers to climate change affected by debris cover. *Nature Geoscience*, *4*(3), 156–159. https://doi.org/10.1038/ngeo1068

Shi, Y. (2002). Characteristics of late Quaternary monsoonal glaciation on the Tibetan Plateau and in East Asia. *Quaternary International*, *97–98*, 79–91. https://doi.org/10.1016/s1040-6182(02)00053-8

Shi, Y. (2005). *Concise glacier catalogue*: Shanghai Science Popularization Press.

Sicart, J. E. (2005). Atmospheric controls of the heat balance of Zongo Glacier (16°S, Bolivia). *Journal of Geophysical Research*, *110*(D12). https://doi.org/10.1029/2004jd005732

Sicart, J. E., Pomeroy, J. W., Essery, R. L. H., & Bewley, D. (2006). Incoming longwave radiation to melting snow: Observations, sensitivity and estimation in Northern environments. *Hydrological Processes*, *20*(17), 3697–3708. https://doi.org/10.1002/hyp.6383

Smeets, C. J. P. P. (2006). Assessing unaspirated temperature measurements using a thermocouple and a physically based model. In *The mass budget of Arctic glaciers* (pp. 99–101). Extended Abstracts-Workshop and GLACIODYN Planning Meeting.

Smeets, C. J. P. P., & van den Broeke, M. R. (2008). The parameterisation of scalar transfer over rough ice. *Boundary-Layer Meteorology*, *128*(3), 339–355. https://doi.org/10.1007/s10546-008-9292-z

Steiner, J. F., Litt, M., Stigter, E. E., Shea, J., Bierkens, M. F. P., & Immerzeel, W. W. (2018). The importance of turbulent fluxes in the surface energy balance of a debris-covered glacier in the Himalayas. *Frontiers of Earth Science*, *6*(144). https://doi.org/10.3389/feart.2018.00144

Stigter, E. E., Litt, M., Steiner, J. F., Bonekamp, P. N. J., Shea, J. M., Bierkens, M. F. P., & Immerzeel, W. W. (2018). The importance of snow sublimation on a Himalayan glacier. *Frontiers of Earth Science*, *6*(108). https://doi.org/10.3389/feart.2018.00108

Sun, W., Qin, X., Du, W., Liu, W., Liu, Y., Zhang, T., et al. (2014). Ablation modeling and surface energy budget in the ablation zone of Laohugou glacier No. 12, western Qilian mountains, China. *Annals of Glaciology*, *55*(66), 111–120. https://doi.org/10.3189/2014AoG66A902

Sun, W., Qin, X., Ren, J., Yang, X., Zhang, T., Liu, Y., et al. (2012). The Surface energy budget in the accumulation zone of the Laohugou Glacier No. 12 in the Western Qilian Mountains, China, in summer 2009. *Arctic, Antarctic, and Alpine Research*, *44*(3), 296–305. https://doi.org/10.1657/1938-4246-44.3.296

Sun, W., Qin, X., Wang, Y., Chen, J., Du, W., Zhang, T., & Huai, B. (2018). The response of surface mass and energy balance of a continental glacier to climate variability, western Qilian Mountains, China. *Climate Dynamics*, *50*, 3557. https://doi.org/10.1007/s00382-017-3823-6

Takahashi, S., Ohata, T., & Yingqin, X. (1989). Characteristics of heat and water fluxes on glacier and ground surfaces in the West Kunlun Mountains. *Bulletin of Glacier Research*, (7), 89–98.

Takeuchi, Y., Kayastha, R. B., & Nakawo, M. (2000). Characteristics of ablation and heat balance in debris-free and debris-covered areas on Khumbu glacier, Nepal Himalayas, in the pre-monsoon season. Paper presented at Debris-Covered Glaciers, IAHS Publications.

Tian, L., Masson-Delmotte, V., Stievenard, M., Yao, T., & Jouzel, J. (2001). Tibetan Plateau summer monsoon northward extent revealed by measurements of water stable isotopes. *Journal of Geophysical Research*, *106*(D22), 28081–28088. https://doi.org/10.1029/2001jd900186

van den Broeke, M. R. (1997). Momentum, heat, and moisture budgets of the katabatic wind layer over a midlatitude glacier in summer. *Journal of Applied Meteorology*, *36*(6), 763–774. https://doi.org/10.1175/1520-0450(1997)036<0763:mhambo>2.0.co;2

van den Broeke, M. R., van As, D., Reijmer, C., & van de Wal, R. (2004), Assessing and improving the quality of unattended radiation observations in Antarctica, *Journal of Atmospheric and Oceanic Technology*, *21*(9), 1417–1431. https://doi.org/10.1175/1520-0426(2004)021<1417:AAITQO>2.0.CO;2

Wagnon, P., Ribstein, P., Francou, B., & Pouyaud, B. (1999). Annual cycle of energy balance of Zongo Glacier, Cordillera Real, Bolivia. *Journal of Geophysical Research*, *104*(D4), 3907–3923. https://doi.org/10.1029/1998jd200011

Wagnon, P., Ribstein, P., Kaser, G., & Berton, P. (1999). Energy balance and runoff seasonality of a Bolivian glacier. *Global and Planetary Change*, *22*(1), 49–58. https://doi.org/10.1016/s0921-8181(99)00025-9

Wagnon, P., Sicart, J. E., Berthier, E., & Chazarin, J. P. (2003). Wintertime high-altitude surface energy balance of a Bolivian glacier, Illimani, 6340 m above sea level. *Journal of Geophysical Research*, *108*(D6). https://doi.org/10.1029/2002jd002088

Wagnon, P., Vincent, C., Arnaud, Y., Berthier, E., Vuillermoz, E., Gruber, S., et al. (2013). Seasonal and annual mass balances of Mera and Pokalde glaciers (Nepal Himalaya) since 2007. *The Cryosphere*, *7*(6), 1769–1786. https://doi.org/10.5194/tc-7-1769-2013

Wal, R. S. W. v. d., & Oerlemans, J. (1994). An energy balance model for the Greenland ice sheet. *Global and Planetary Change*, *9*, 115–131.

Wang, M. (1962). Overview of the physical geography around Mt. Qomolangma. In T. C. s. e. t. i. M. Qomolangma (Ed.), *Report of scientific expedition in Mt. Qomolangma (in Chinese)* (p. 291). Science Press.

Wang, N., He, J., Pu, J., Jiang, X., & Jing, Z. (2010). Variations in equilibrium line altitude of the Qiyi Glacier, Qilian Mountains, over the past 50 years. *Chinese Science Bulletin*, *55*(33), 3810–3817. https://doi.org/10.1007/s11434-010-4167-3

Weiss, A. (1981). On the performance of pyrgeometers with silicon domes. *Journal of Applied Meteorology*, *20*(8), 962–965. https://doi.org/10.1175/1520-0450(1981)0202.0.CO10.1175/1520-0450(1981)020<0962:otpopw>2.0.co;2

Xiao, C., Liu, S., Zhao, L., Wu, Q., LI, P., Liu, C., et al. (2007). Observed changes of cryosphere in China over the second half of the 20th century: An overview. *Annals of Glaciology*, *46*(1), 382–390. https://doi.org/10.3189/172756407782871396

Xu, B., Cao, J., Hansen, J., Yao, T., Joswia, D. R., Wang, N., et al. (2009). Black soot and the survival of Tibetan glaciers. *Pnas*, *106*(52), 22114–22118. https://doi.org/10.1073/pnas.0910444106

Yang, K., Koike, T., Fujii, H., Tamagawa, K., & Hirose, N. (2002). Improvement of surface flux parametrizations with a turbulence-related length. *Quarterly Journal of the Royal Meteorological Society*, *128*(584), 2073–2087. https://doi.org/10.1256/003590002320603548

Yang, W., Guo, X., Yao, T., Yang, K., Zhao, L., Li, S., & Zhu, M. (2011). Summertime surface energy budget and ablation modeling in the ablation zone of a maritime Tibetan glacier. *Journal of Geophysical Research*, *116*(D14). https://doi.org/10.1029/2010jd015183

Yang, W., Guo, X., Yao, T., Zhu, M., & Wang, Y. (2016). Recent accelerating mass loss of southeast Tibetan glaciers and the relationship with changes in macroscale atmospheric circulations. *Climate Dynamics*, *47*(3), 805–815. https://doi.org/10.1007/s00382-015-2872-y

Yang, W., Yao, T., Guo, X., Zhu, M., Li, S., & Kattel, D. B. (2013). Mass balance of a maritime glacier on the southeast Tibetan Plateau and its climatic sensitivity. *Journal of Geophysical Research: Atmospheres*, *118*(17), 9579–9594. https://doi.org/10.1002/jgrd.50760

Yang, X. (2010). Characteristics of meteorological elements and impact on glacier's change on the north slope of the Mt. Qomolangma Region (Dissertation thesis, p. 125). Cold and Arid Regions Environmental and Engineering Research Institute, Chinese Academy of Sciences.

Yang, X., Zhang, T., Qin, D., Kang, S., & Qin, X. (2011). Characteristics and changes in air temperature and glacier's response on the north slope of Mt. Qomolangma (Mt. Everest). *Arctic, Antarctic, and Alpine Research*, *43*(1), 147–160. https://doi.org/10.1657/1938-4246-43.1.147

Yang, X., Zhang, T., Qin, D., Qin, X., & Yang, Y. (2015). Observational study of surface wind regime on the North Slope of Mount Qomolangma (Mount Everest). *Arctic, Antarctic, and Alpine Research*, *47*(4), 807–817. https://doi.org/10.1657/aaar00c-13-132

Yao, T., Li, Z., Yang, W., Guo, X., Zhu, L., Kang, S., et al. (2010). Glacial distribution and mass balance in the Yarlung Zangbo River and its influence on lakes. *Chinese Science Bulletin*, *55*(1001–6538), 2072. https://doi.org/10.1007/s11434-010-3213-5

Yao, T., Pu, J., Lu, A., Wang, Y., & Yu, W. (2007). Recent glacial retreat and its impact on hydrological processes on the Tibetan Plateau, China, and surrounding regions. *Arctic, Antarctic, and Alpine Research*, *39*(4), 642–650. https://doi.org/10.1657/1523-0430(07-510)[yao]2.0.co;2

Yao, T., Thompson, L., Yang, W., Yu, W., Gao, Y., Guo, X., et al. (2012). Different glacier status with atmospheric circulations in Tibetan Plateau and surroundings. *Nature Climate Change*, *2*(9), 663–667. https://doi.org/10.1038/nclimate1580

Ye, Q., Bolch, T., Naruse, R., Wang, Y., Zong, J., Wang, Z., et al. (2015). Glacier mass changes in Rongbuk catchment on Mt. Qomolangma from 1974 to 2006 based on topographic maps and ALOS PRISM data. *Journal of Hydrology*, *530*, 273–280. https://doi.org/10.1016/j.jhydrol.2015.09.014

Ye, Q., Zhong, Z., Kang, S., Stein, A., Wei, Q., & Liu, J. (2009). Monitoring glacier and supra-glacier lakes from space in Mt. Qomolangma region of the Himalayas on the Tibetan Plateau in China. *Journal of Mountain Science*, *6*(3), 211–220. https://doi.org/10.1007/s11629-009-1016-4

Ye, Q., Zong, J., Tian, L., Cogley, J. G., Song, C., & Guo, W. (2017). Glacier changes on the Tibetan Plateau derived from Landsat imagery: Mid-1970s-2000-13. *Journal of Glaciology*, *63*(238), 273–287. https://doi.org/10.1017/jog.2016.137

You, Q., Kang, S., Pepin, N., Flügel, W.-A., Sanchez-Lorenzo, A., Yan, Y., & Zhang, Y. (2010). Climate warming and associated changes in atmospheric circulation in the eastern and central Tibetan Plateau from a homogenized dataset. *Global and Planetary Change*, *72*(1), 11–24. https://doi.org/10.1016/j.gloplacha.2010.04.003

Yu, W., Yao, T., Kang, S., Pu, J., Yang, W., Gao, T., et al. (2013). Different region climate regimes and topography affect the changes in area and mass balance of glaciers on the north and south slopes of the same glacierized massif (the West Nyainqentanglha Range, Tibetan Plateau). *Journal of Hydrology*, *495*, 64–73. https://doi.org/10.1016/j.jhydrol.2013.04.034

Zhang, D., Qin, D., Hou, S., Kang, S., & Ren, J. (2004). Net accumulation rate of the East Rongbuk glacier and Indian summer monsoon rainfall. *Journal of Glaciology and Geocryology*, *26*(4), 129–134.

Zhang, G., Kang, S., Fujita, K., Huintjes, E., Xu, J., Yamazaki, T., et al. (2013). Energy and mass balance of Zhadang glacier surface, central Tibetan Plateau. *Journal of Glaciology*, *59*(213), 137–148. https://doi.org/10.3189/2013JoG12J152

Zhang, Y., Liu, S., Ding, Y., Li, J., & Shangguan, D. (2006). Preliminary study of mass balance on the Keqicar Baxi glacier on the south slopes of Tianshan Mountains. *Journal of Glaciology and Geocryology*, *28*(4), 477–484.[in Chinese].

Zhang, Y., Yao, T., Pu, J., Ohata, T., Yabuki, H., & Fujita, K. (1996). Energy budget at ELA on Dongkemadi Glacier in the Tanggula Mts. Tibetan Plateau. *Journal of Glaciology and Geocryology*, *18*(1), 10–19.

Zhou, Y., Li, Z., & Li, J. (2017). Slight glacier mass loss in the Karakoram region during the 1970s to 2000 revealed by KH-9 images and SRTM DEM. *Journal of Glaciology*, *63*(238), 331–342. https://doi.org/10.1017/jog.2016.142

Zhu, M., Yao, T., Yang, W., Maussion, F., Huintjes, E., & Li, S. (2015). Energy- and mass-balance comparison between Zhadang and Parlung No. 4 glaciers on the Tibetan Plateau. *Journal of Glaciology*, *61*(227), 595–607. https://doi.org/10.3189/2015JoG14J206

Zou, H., Ma, S., Zhou, L., Li, P., & Li, A. (2009). Measured turbulent heat transfer on the northern slope of Mt. Everest and its relation to the south Asian summer monsoon. *Geophysical Research Letters*, *36*(9). https://doi.org/10.1029/2008gl036984